UNIVERSITY OF OKLAHOMA

GRADUATE COLLEGE

INVESTIGATION OF SPECIAL PROBLEMS IN ELECTROMAGNETICS WITH THE FINITE-DIFFERENCE TIME-DOMAIN METHOD

A THESIS

SUBMITTED TO THE GRADUATE FACULTY

in partial fulfillment of the requirements for the

Degree of

MASTER OF SCIENCE

By

MARK CASH
Norman, Oklahoma
2024

INVESTIGATION OF SPECIAL PROBLEMS IN ELECTROMAGNETICS WITH THE FINITE-DIFFERENCE TIME-DOMAIN METHOD

A THESIS APPROVED FOR THE
SCHOOL OF ELECTRICAL AND COMPUTER ENGINEERING

BY THE COMMITTEE CONSISTING OF

Dr. Jessica Ruyle, Chair

Dr. Justin Metcalf

Dr. Nathan Goodman

Acknowledgments

I want to start by thanking my advisor Dr. Jessica Ruyle for giving me the confidence to even do this in the first place, for her endless patience and support, and for her advice on academic and research matters.

Next, I would like to thank Clayton Blosser for his friendship and mentorship, without which I probably would have been overwhelmed at the beginning of the program. I also would like to thank the Ruyle Research Group, including Rosalind Agasti, Mariel Avalos, Adrian Bauer, Andrew Eck, MacKenzie Kelsoe, William Van Houten, and many others for their support and for putting up with my awful practice talks.

Thank you to my parents for a lifetime of support, encouragement, and for fostering my passion for science at a young age. To my brother Michael, thank you for believing in me even when I don't. To the love of my life, Lucy, I would not have made it this far without you. Taking that silly Astronomy class that I didn't even need ranks as the best decision I have ever made because it led me to you. Thank you to my kids Zoey and Zander, I couldn't have asked for a better family and I love you both. And finally I would like to thank my cat Luna, for keeping me company during endless hours of reading, coding, and writing.

This effort was sponsored in whole or in part by the United States Government (USG). The U.S. Government is authorized to reproduce and distribute original submissions for publication for Governmental purposes notwithstanding any copyright notation thereon. The views and conclusions contained herein are those of the authors and should not be interpreted as necessarily representing the official policies or endorsements, either expressed or implied, of the United States Government (USG).

Table of Contents

Acknowledgment **iv**

List of Figures **viii**

List of Tables **xi**

Abstract **xii**

1 Introduction **1**

1.1 Background 1

1.1.1 Non-LTI Antennas 2

1.1.2 Human Head Modeling at RF and Microwave Frequencies 3

2 Finite-Difference Time-Domain Method **4**

2.1 Introduction to FDTD 4

2.2 Maxwell's Equations and the Yee Algorithm 5

2.3 Numerical Dispersion 11

2.4 Stability Conditions 14

2.5 Lumped Components 18

2.6 Boundary Conditions 19

2.7 Conclusions 22

3 Time-Varying Antenna Loads **23**

3.1 Time-Varying Components in FDTD 24

3.1.1 Switched Loads 24

3.1.2 Simulation of Switched Loads 25

3.1.3 Time-Varying Capacitive Load 27

3.1.4 Simulation of Time-Varying Capacitive Loads 29

3.2 Discussion 37

4 Modeling the Human Head at Radio Frequencies **39**

4.1 Dispersive Material Modeling 39

4.2 Simulation Results 46

4.3 Discussion 59

5 Conclusions and Future Work **61**

5.1 Conclusions 61

5.2 Scientific Impact 61

5.3 Future Work 62

List of Figures

2.1 Cubic unit Yee spatial cell. Electric field components in blue. Magnetic field components in red. 8

2.2 Refractive index components along the x and y axis showing isotropic dispersion. Time-step is selected by $\Delta t = \frac{1}{N_t f}$ Spatial-step is set to $\Delta l = \frac{\lambda}{10}$. 13

2.3 Phase portrait of the refractive index along the x and y axis showing anisotropic dispersion. Spatial-step is selected by$\Delta l = \frac{\lambda}{N_\lambda}$ Time-step is set to $\Delta t = \frac{1}{10f}$. 13

2.4 1-D FDTD grid with the edge Ez component labeled. 19

2.5 1-D FDTD grid with the edge Ez component labeled. 20

3.1 100MHz switch waveform with a transition period in the time-domain(top) and frequency-domain(bottom) 25

3.2 Ribbon dipole antenna. $R_F = 50\Omega$, $D = 15cm$, $W = 0.5cm$ with a plane wave excitation of 100MHz. $d = 208mm \approx \frac{\lambda}{14}$. 25

3.3 Time and frequency domain currents across the resistor representing the dipole feed for a switch loaded dipole with switch transition times of 1 timestep and 60 timesteps. 26

3.4 Time and frequency domain currents at the feed for a switch loaded dipole. Incident plane wave at 1GHz and switching frequency of 100MHz. Simulated in OU-FDTD and XFDTD. 27

3.5 Loop Antenna. $R_F = 26\Omega$, $C_0 = 2.7pF$, $\gamma = 0.6$, f_p = 195MHz, $\phi = 0$, with a plane wave excitation of 100MHz. $d = 208mm \approx \frac{\lambda}{14}$. 30

3.6 Time domain current across the feed resistor (R_F in Figure 3.5). Simulated in CM-MoM, CST Studio, and OU-FDTD. Truncated to first steady-state period. 31

3.7 Time domain results showing a 6MHz beat frequency. 32

3.8 Power received over an excitation frequency sweep for the first time time-varying capacitor antenna design. LTI comparison is a conjugate match with $R_F = 6$ and $C_0 = 4.0pF$. 33
3.9 Power received around the excitation frequency(top) and the first sum harmonic (bottom) for the upconversion design listed in Table 3.2 35
3.10 On-off key modulation scheme. Pulse width of 500ns. 36
3.11 Time domain current across the feed resistor (R_F in Figure 3.5). (a) Non-LTI antenna design, and (b) LTI antenna design. Simulated in CST Studio. . . . 37

4.1 Modeled and measured effective dielectric constant for four different human tissues. 42
4.2 Cut planes of the head phantoms coplanar with the ear canal. Color coded by unique tissue ID. (a) MIDA model. (b) Duke model. 45
4.3 Time and frequency domain representations of the LFM waveforms used in this work. (a) LFM1: $\beta = 400$MHz, $\tau = 150$ns. (b) LFM2: $\beta = 840$MHz, $\tau = 150$ns. 46
4.4 Electric field amplitude relative to the incident plane wave(LFM1) within the MIDA model simulated in OU-FDTD. Cross-sectional view(coplanar with the ear canal) shown at peak amplitude. 47
4.5 Electric field amplitude relative to the incident plane wave(LFM1) within the MIDA model simulated in OU-FDTD. Shown at various cross-sectional views. (a) Coplanar with the ear canal. (b) 25mm up from the ear canal. (c) 50mm up from the ear canal. (d) 75mm up from the ear canal. 48
4.6 Electric field amplitude relative to the incident plane wave within the MIDA model simulated in OU-FDTD. Point-sensor located in fat tissue. Results from LFM1 and LFM2. 49
4.7 Electric field amplitude relative to the incident plane wave within the MIDA model simulated in OU-FDTD. Shown at various time-steps throughout the simulation of LFM2. (a) t = 109.2 ns. (b) t = 109.6 ns. (c) t = 109.9 ns. (d) t = 110.3 ns. 50
4.8 Electric field amplitude relative to the incident plane wave(LFM2) within the MIDA model simulated in OU-FDTD and XFDTD. Shown at time-step of peak amplitude. (a) OU-FDTD. (b) XFDTD. 51

4.9 Electric field amplitude relative to the incident plane wave(LFM2) within the MIDA model simulated in OU-FDTD and XFDTD. Point-sensor located in adipose tissue. 52
4.10 Electric field amplitude relative to the incident plane wave(LFM2) within the MIDA and Duke models simulated in OU-FDTD. Shown at time-step of peak amplitude. (a) MIDA. (b) Duke. 52
4.11 Electric field amplitude relative to the incident plane wave(LFM2) within the Duke model simulated in OU-FDTD. Shown at various cross-sectional views. (a) Coplanar with the ear canal. (b) 25mm up from the ear canal. (c) 50mm up from the ear canal. (d) 75mm up from the ear canal. 54
4.12 Electric field amplitude relative to the incident plane wave within the Duke model simulated in OU-FDTD. Shown at various time-steps throughout the simulation of LFM2. (a) t = 93.2 ns. (b) t = 93.6 ns. (c) t = 94.0 ns. (d) t = 94.4 ns. (e) Electric field amplitude relative to the incident plane wave at a point sensor located within fat tissue. Red markers indicate the time-steps shown in panels (a)-(d). 55
4.13 Electric field amplitude relative to the incident plane wave(LFM2) within the full-size and half-size MIDA model simulated in OU-FDTD. Shown at time-step of peak amplitude. (a) Full-size. (b) Half-size. 56
4.14 Electric field amplitude relative to the incident plane wave(LFM2) within the half-size Mida model simulated in OU-FDTD. Shown at various cross-sectional views. (a) Coplanar with the ear canal. (b) 17mm up from the ear canal. (c) 34mm up from the ear canal. (d) 51mm up from the ear canal. . . 57
4.15 Electric field amplitude relative to the incident plane wave within the half-size MIDA model simulated in OU-FDTD. Shown at various time-steps throughout the simulation of LFM2. (a) t = 145.03 ns. (b) t = 145.20 ns. (c) t = 145.37 ns. (d) t = 145.50 ns. (e) Electric field amplitude relative to the incident plane wave at a point sensor located within adipose tissue. Red markers indicate the time-steps shown in panels (a)-(d). 58
4.16 Electric field amplitude relative to the incident plane wave(LFM2) within the full-size and half-size MIDA models simulated in OU-FDTD. Point-sensor located in adipose tissue. 59

List of Tables

3.1 Design parameters for the first time-varying capacitor antenna design. . . . 32
3.2 Design parameters for the second time-varying capacitor antenna design. . . 34
3.3 Design parameters for the third time-varying capacitor antenna design. . . . 35

4.1 Debye Parameters for Human Tissue (100MHz-5GHz) 44

Abstract

The Finite-Difference Time-Domain(FDTD) method is a robust numerical time-domain technique capable of handling a broad range of electromagnetic problems. This work explores the application of FDTD method to two special problems in electromagnetics: the modeling of antennas loaded with time-varying components, and the modeling of the human head at microwave frequencies.

A recent surge in interest for non-LTI antennas – driven by a desire to circumvent the performance bounds of their LTI counterparts – has made apparent the need for modeling techniques capable of handling nonlinear or time-variant behavior on antenna structures. Modeling of time-varying components in FDTD will be demonstrated through direct implantation in the FDTD algorithm with a modified update equation, and through SPICE co-simulation.

There is currently a large body of work studying the impact of microwave and radio frequency radiation on human tissue. The effects of prolonged exposure to non-ionizing radiation is typically characterized using specific absorption rate (SAR), and research has often been conducted in the context of wireless communication devices. Many papers in open literature involve simulations with a source antenna in close proximity to the head, excited by a single tone continuous wave or narrow-band gaussian pulses. Using relaxation models to account for the frequency dependent behavior of tissue, this work investigates the interactions of plane waves excited by linear-frequency modulated pulses incident upon the human head in FDTD.

Chapter 1

Introduction

1.1 Background

Computational electromagnetic modeling (CEM) techniques can be broadly grouped into two categories, frequency-domain and time-domain. Frequency-domain methods solve Maxwell's equations at discrete frequencies and are highly effective for analyzing steady-state behavior and modal analysis. By contrast, time-domain methods simulate the marching of Maxwell's equations through time, allowing for the capture of transient behaviors. Among the many numerical methods employed in CEM, the finite-difference (FD), finite element (FE), and method of moments (MoM) techniques are widely used in both time and frequency domain analysis. Finite element and finite difference methods are capable of discretizing space over a volume, while method-of-moments solves problems in one or two dimensions. One of the most widely used time-domain methods is the Finite-Difference Time-Domain method, which utilizes central difference approximations to discretize Maxwell's equations, and advances them through time with a leap-frog scheme [1]. The FDTD method is popular for its ability to model a wide variety of phenomena while maintaining simplicity in its implementation. Nonlinear and time-variant behavior, as well as inhomogeneous media are handled naturally in FDTD, making it an ideal choice for modeling the two problems described in this thesis. Chapter 2 of this thesis will describe the general FDTD method that was used to build a solver in the MATLAB programming language, described throughout the rest of this work as OU-FDTD.

1.1.1 Non-LTI Antennas

RF and microwave devices are often constrained to be linear and time-invariant(LTI) to simplify the math governing their design, analysis, and characterization. These constraints have historically been included in the analysis of performance bounds for electrically small antennas [2], [3] , which has made the idea of circumventing these bounds by breaking the LTI assumption appealing to many researchers. Advances in the capabilities of computing systems, such as increased memory capacities, hardware acceleration with graphics processing units, and multicore central processing units have also made the numerical modeling of non-LTI antennas a more appealing prospect. There has been a score of recent work in this developing field focusing on rapidly varying properties of the antenna aperture [4], [5], [6], [7]. These proposed methods maintain linearity, but introduce a time-variance into the system. In Chapter 3, methods for modeling time-varying components in FDTD will be discussed and then applied to several antenna designs. The results from OU-FDTD in this chapter are compared to two commercial time-domain solvers, Simulia's CST Studio [8], and Remcom's XFDTD [9]. The current shortcomings of these two commercial solvers when it comes to modeling time-varying components are made clear. A frequency-domain solver, conversion matrix method of moments (CM-MoM) [10] is also utilized for comparison. The strengths and weaknesses of CM-MoM and FDTD are discussed, as well as how they can be used in conjunction to design and fully analyze a non-LTI antenna.

1.1.2 Human Head Modeling at RF and Microwave Frequencies

The growth of mobile communications platforms over the last two decades has motivated an increasing interest in accurately modeling the interaction of non-ionizing electromagnetic radiation with human tissue. In place of human testing, analysis in this area is largely done with time domain electromagnetic solvers such as FDTD. This research is typically conducted in the context of evaluating SAR distributions due to an antenna placed close to the human head [11], [12]. Head phantoms used in this analysis range from simple sphere models that use an average permittivity, conductivity, and mass density[13], to higher detailed models constructed from voxelized MRI data [14]. Human tissue itself is a dispersive material [15], which means that its relative permittivity and conductivity are frequency dependent parameters. Chapter 4 describes one of the methods used for modeling this frequency dependent behavior in OU-FDTD, and demonstrates it in the analysis of two human head phantoms.

Chapter 2

Finite-Difference Time-Domain Method

This chapter will provide background on the FDTD method and introduce the core concepts behind its formulation. Key aspects related to the problems posed in this thesis such as numerical dispersion, stability, and dispersive materials will be highlighted.

2.1 Introduction to FDTD

The Finite-Difference Time-Domain algorithm was first presented by Kane Yee as a numerical method for modeling electromagnetic phenomena in the time domain [1]. Improvements in the capabilities of computer processors coupled with the algorithm's simplistic implementation have made it a popular tool among research scientists and engineers. It's commonly used in radar, communications, and biomedical problems.

Initially introduce as the ”Yee algorithm,” Allen Taflove coined the FDTD acronym in a 1980 paper which validated FDTD models for sinusodial steady-state waves in a three-dimensional cavity [16]. FDTD's capabilities were greatly developed in the late 80's into the early 90's as researchers utilized it to model a broad range of electromagnetic problems [17–22]. More recent developments include updates to the algorithm for more efficient statistical analysis [23], a thin wire approximation for for conductors [24], and a least-squares algorithm for timesteps that break the Courant-Friedrichs-Lewy limit [25].

The FDTD method takes Maxwell's curl equations in their differential form and discretizes them, implementing a time-dependent solution with central difference approximations. To preserve second-order accuracy, the electric and magnetic fields are staggered in both space and time. The fields are updated throughout the domain in terms of past field values, using the leap-frog numerical scheme to incrementally march the electric and magnetic fields through time. While the FDTD method can be solved on a number of different grid geometries, this thesis utilizes the Cartesian-grid used in Yee's initial formulation of the algorithm.

2.2 Maxwell's Equations and the Yee Algorithm

To simplify analysis, this section presumes propagation in an isotropic and homoegenous medium, which will change in Chapter 4 when considering the dispersive effects of human tissues. Furthermore, we assume no electric or magnetic sources. The time-dependent Maxwell's equations in differential form are given by

$$\nabla \times \boldsymbol{E} = -\frac{\partial \boldsymbol{B}}{\partial t} - \boldsymbol{M}, \tag{2.1a}$$

$$\nabla \times \boldsymbol{H} = \frac{\partial \boldsymbol{D}}{\partial t} + \boldsymbol{J}, \tag{2.1b}$$

$$\nabla \cdot \boldsymbol{D} = \boldsymbol{\rho} \text{ and} \tag{2.1c}$$

$$\nabla \cdot \boldsymbol{B} = 0. \tag{2.1d}$$

The vectors are space-time functions of the form (x, y, z, t). The material properties for the propagation medium are applied through the constitutive relations, which in their general form are given by

$$\boldsymbol{D} = [\epsilon(t)] \circledast \boldsymbol{E} \text{ and} \tag{2.2a}$$

$$\boldsymbol{B} = [\mu(t)] \circledast \boldsymbol{H}. \tag{2.2b}$$

In the general case for dispserive and anisotropic materials, the electric flux density and magnetic flux density are related to their field counterparts through a convolution of a time-varying permittivity or permeability tensor. For isotropic and non-dispersive materials, the permittivity and permeability can be represented by a time-invariant constant which simplifies the constitutive relations to

$$\boldsymbol{D} = \epsilon \boldsymbol{E} \text{ and} \tag{2.3a}$$

$$\boldsymbol{B} = \mu \boldsymbol{H}. \tag{2.3b}$$

For lossy materials $\boldsymbol{J}$ and $\boldsymbol{M}$ in (2.1b) and (2.1a) relate to their respective fields as

$$\boldsymbol{J} = \sigma \boldsymbol{E} \text{ and} \tag{2.4a}$$

$$\boldsymbol{M} = \sigma^{*} \boldsymbol{H} \tag{2.4b}$$

where σ is electrical conductivity and σ^{*} is an equivalent magnetic loss term.

To form Maxwell's equations for linear, non-dispserive, isotropic, and lossy materials we then substitute (2.3) and (2.4) into (2.1a) and (2.1b), which yields

$$\frac{\partial \boldsymbol{H}}{\partial t} = -\frac{1}{\mu}\nabla \times \boldsymbol{E} - \frac{1}{\mu}\boldsymbol{\sigma}^{*}\boldsymbol{H} \text{ and} \tag{2.5a}$$

$$\frac{\partial \boldsymbol{E}}{\partial t} = -\frac{1}{\mu}\nabla \times \boldsymbol{H} - \frac{1}{\mu}\boldsymbol{\sigma}\boldsymbol{E}. \tag{2.5b}$$

Writing out the vector components after applying the curl operators then gives a system of coupled scalar equations

$$\frac{\partial E_x}{\partial t} = \frac{1}{\epsilon}\left[\frac{\partial H_z}{\partial y} - \frac{\partial H_y}{\partial z} - \sigma E_x\right] \tag{2.6a}$$

$$\frac{\partial E_y}{\partial t} = \frac{1}{\epsilon}\left[\frac{\partial H_x}{\partial z} - \frac{\partial H_z}{\partial x} - \sigma E_y\right] \tag{2.6b}$$

$$\frac{\partial E_z}{\partial t} = \frac{1}{\epsilon}\left[\frac{\partial H_y}{\partial x} - \frac{\partial H_x}{\partial y} - \sigma E_z\right] \tag{2.6c}$$

$$\frac{\partial H_x}{\partial t} = \frac{1}{\mu}\left[\frac{\partial E_y}{\partial z} - \frac{\partial E_z}{\partial y} - \sigma^{*} H_x\right] \tag{2.6d}$$

$$\frac{\partial H_y}{\partial t} = \frac{1}{\mu}\left[\frac{\partial E_z}{\partial x} - \frac{\partial E_x}{\partial z} - \sigma^{*} H_y\right] \tag{2.6e}$$

$$\frac{\partial H_z}{\partial t} = \frac{1}{\mu}\left[\frac{\partial E_x}{\partial y} - \frac{\partial E_y}{\partial x} - \sigma^{*} H_z\right], \tag{2.6f}$$

which when combined with central difference approximations, form the basis of the FDTD algorithm. This thesis will use the notation $E^{n}_{x(i,j,k)} = E(i\Delta x, j\Delta y, k\Delta z, n\Delta t)$ for the scalar electric and magnetic field components. Where i, j, k describe the spatial coordinates of the corresponding fied component, and n describes its time-step. As shown in Fig. 2.1, the FDTD spatial lattice is structured such that $\boldsymbol{E}$ components are surrounded by four curling $\boldsymbol{H}$ components, and $\boldsymbol{H}$ components are surrounded by four curling $\boldsymbol{E}$ components. $\boldsymbol{E}$ and $\boldsymbol{H}$ components are similarly staggered in time using a leap-frog scheme. The $\boldsymbol{E}$ field computations are completed using previous $\boldsymbol{H}$ field data. Next, the $\boldsymbol{H}$ field computations are completed using the $\boldsymbol{E}$ fields computed in the last step. This process repeats until the algorithm is terminated via a convergence or time condition.

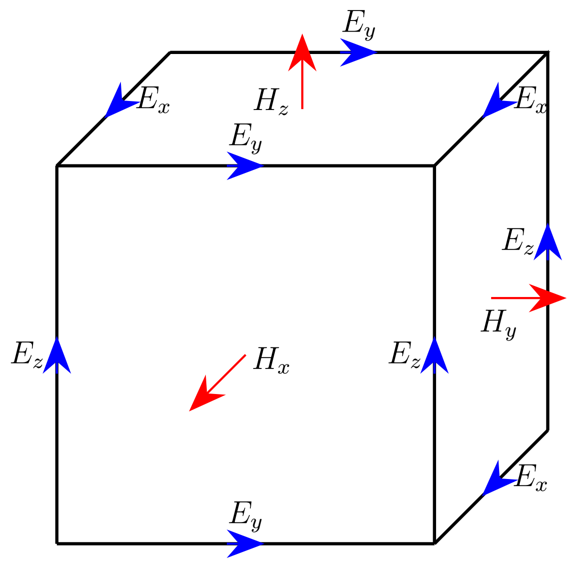

Figure 2.1: Cubic unit Yee spatial cell. Electric field components in blue. Magnetic field components in red.

The FDTD algorithm utilizes central difference approximations for the space and time derivatives given in (2.6). Applying central difference approximation to a partial spatial derivative in the x-direction yields

$$\frac{\partial u}{\partial x}(i\Delta x, j\Delta y, k\Delta z, n\Delta t) = \frac{u^n_{(i+\frac{1}{2},j,k)} - u^n_{(i-\frac{1}{2},j,k)}}{\Delta x} + O[(\Delta x)^2], \tag{2.7}$$

and applied to a partial time derivative

$$\frac{\partial u}{\partial t}(i\Delta x, j\Delta y, k\Delta z, n\Delta t) = \frac{u^{n+\frac{1}{2}}_{(i,j,k)} - u^{n-\frac{1}{2}}_{(i,j,k)}}{\Delta t} + O[(\Delta t)^2]. \tag{2.8}$$

Applying (2.7) and (2.8) to the first equation in Equation (2.6) will give

$$\begin{aligned}\frac{1}{\Delta t}\Big(E^{n+\frac{1}{2}}_{x(i,j+\frac{1}{2},k+\frac{1}{2})} - E^{n-\frac{1}{2}}_{x(i,j+\frac{1}{2},k+\frac{1}{2})}\Big) = &\frac{1}{\epsilon_{x(i,j+\frac{1}{2},k+\frac{1}{2})}}\Big(\frac{H^n_{z(i,j+1,k+\frac{1}{2})} - H^n_{z(i,j,k+\frac{1}{2})}}{\Delta y}\Big) \\ &- \frac{1}{\epsilon_{x(i,j+\frac{1}{2},k+\frac{1}{2})}}\Big(\frac{H^n_{y(i,j+\frac{1}{2},k+1)} - H^n_{z(i,j+\frac{1}{2},k)}}{\Delta x}\Big) \\ &- \frac{1}{\epsilon_{x(i,j+\frac{1}{2},k+\frac{1}{2})}}\Big(\sigma_{(i,j+\frac{1}{2},k+\frac{1}{2})}E^n_{x(i,j+\frac{1}{2},k+\frac{1}{2})}\Big).\end{aligned} \tag{2.9}$$

In order to fix the E_x component appearing with the material conductivity σ to the correct temporal grid, a semi-implicit approximation is used

$$E^n_{x(i,j+\frac{1}{2},k+\frac{1}{2})} = \frac{E^{n+\frac{1}{2}}_{x(i,j+\frac{1}{2},k+\frac{1}{2})} + E^{n-\frac{1}{2}}_{x(i,j+\frac{1}{2},k+\frac{1}{2})}}{2}. \tag{2.10}$$

After substituting this approximation into (2.9) and collecting like terms, we find the desired update equation for the E_x component

$$\begin{aligned}E^{n+\frac{1}{2}}_{x(i,j+\frac{1}{2},k+\frac{1}{2})} = &\Bigg(\frac{1 - \frac{\sigma_{(i,j+\frac{1}{2},k+\frac{1}{2})}\Delta t}{2\epsilon_{(i,j+\frac{1}{2},k+\frac{1}{2})}}}{1 + \frac{\sigma_{(i,j+\frac{1}{2},k+\frac{1}{2})}\Delta t}{2\epsilon_{(i,j+\frac{1}{2},k+\frac{1}{2})}}}\Bigg)E^{n-\frac{1}{2}}_{x(i,j+\frac{1}{2},k+\frac{1}{2})} \\ &+ \frac{\Delta t}{2\epsilon_{(i,j+\frac{1}{2},k+\frac{1}{2})}}\Big(\frac{H^n_{z(i,j+1,k+\frac{1}{2})} - H^n_{z(i,j,k+\frac{1}{2})}}{\Delta y} - \frac{H^n_{y(i,j+\frac{1}{2},k+1)} - H^n_{z(i,j+\frac{1}{2},k)}}{\Delta x}\Big).\end{aligned} \tag{2.11}$$

The rest of the update equations are derived following the same process. For a cubic spatial lattice, $\Delta x = \Delta y = \Delta z = \Delta l$. The material property terms containing σ, ϵ, σ^*, and μ can be collected into coefficients and the update equation simplified to

$$\begin{aligned} E^{n+\frac{1}{2}}_{x(i,j+\frac{1}{2},k+\frac{1}{2})} &= C_{ax(i,j+\frac{1}{2},k+\frac{1}{2})} E^{n-\frac{1}{2}}_{x(i,j+\frac{1}{2},k+\frac{1}{2})} \\ &+ C_{bx(i,j+\frac{1}{2},k+\frac{1}{2})} \begin{pmatrix} H^n_{z(i,j+1,k+\frac{1}{2})} - H^n_{z(i,j,k+\frac{1}{2})} + \\ H^n_{y(i,j+\frac{1}{2},k)} - H^n_{z(i,j+\frac{1}{2},k+1)} \end{pmatrix} \end{aligned} \tag{2.12a}$$

$$\begin{aligned} E^{n+\frac{1}{2}}_{y(i-\frac{1}{2},j+1,k+\frac{1}{2})} &= C_{ay(i-\frac{1}{2},j+1,k+\frac{1}{2})} E^{n-\frac{1}{2}}_{y(i-\frac{1}{2},j+1,k+\frac{1}{2})} \\ &+ C_{by(i-\frac{1}{2},j+1,k+\frac{1}{2})} \begin{pmatrix} H^n_{x(i-\frac{1}{2},j+1,k+1)} - H^n_{x(i-\frac{1}{2},j+1,k)} + \\ H^n_{z(i-1,j+1,k+\frac{1}{2})} - H^n_{z(i,j+1,k+\frac{1}{2})} \end{pmatrix} \end{aligned} \tag{2.12b}$$

$$\begin{aligned} E^{n+\frac{1}{2}}_{z(i-\frac{1}{2},j+\frac{1}{2},k+1)} &= C_{az(i-\frac{1}{2},j+\frac{1}{2},k+1)} E^{n-\frac{1}{2}}_{z(i-\frac{1}{2},j+\frac{1}{2},k+1)} \\ &+ C_{bz(i-\frac{1}{2},j+\frac{1}{2},k+1)} \begin{pmatrix} H^n_{y(i,j+\frac{1}{2},k+1)} - H^n_{y(i-1,j+\frac{1}{2},k+1)} + \\ H^n_{x(i-\frac{1}{2},j,k+1)} - H^n_{x(i-\frac{1}{2},j+1,k+1)} \end{pmatrix} \end{aligned} \tag{2.12c}$$

$$\begin{aligned} H^{n+1}_{x(i-\frac{1}{2},j+1,k+1)} &= D_{ax(i-\frac{1}{2},j+1,k+1)} H^n_{x(i-\frac{1}{2},j+1,k+1)} \\ &+ D_{bx(i-\frac{1}{2},j+1,k+1)} \begin{pmatrix} E^{n+\frac{1}{2}}_{y(i-\frac{1}{2},j+1,k+\frac{3}{2})} - E^{n+\frac{1}{2}}_{y(i-\frac{1}{2},j+1,k+\frac{1}{2})} + \\ E^{n+\frac{1}{2}}_{z(i-\frac{1}{2},j+\frac{1}{2},k+1)} - E^{n+\frac{1}{2}}_{z(i-\frac{1}{2},j+\frac{3}{2},k+1)} \end{pmatrix} \end{aligned} \tag{2.12d}$$

$$\begin{aligned} H^{n+1}_{y(i,j+\frac{1}{2},k+1)} &= D_{ay(i,j+\frac{1}{2},k+1)} H^n_{y(i,j+\frac{1}{2},k+1)} \\ &+ D_{by(i,j+\frac{1}{2},k+1)} \begin{pmatrix} E^{n+\frac{1}{2}}_{z(i+\frac{1}{2},j+\frac{1}{2},k+1)} - E^{n+\frac{1}{2}}_{z(i-\frac{1}{2},j+\frac{1}{2},k+1)} + \\ E^{n+\frac{1}{2}}_{x(i,j+\frac{1}{2},k+\frac{1}{2})} - E^{n+\frac{1}{2}}_{x(i,j+\frac{1}{2},k+1)} \end{pmatrix} \end{aligned} \tag{2.12e}$$

$$\begin{aligned} H^{n+1}_{z(i,j+1,k+\frac{1}{2})} &= D_{az(i,j+1,k+\frac{1}{2})} H^n_{z(i,j+1,k+\frac{1}{2})} \\ &+ D_{bz(i,j+1,k+\frac{1}{2})} \begin{pmatrix} E^{n+\frac{1}{2}}_{x(i,j+\frac{3}{2},k+\frac{1}{2})} - E^{n+\frac{1}{2}}_{x(i,j+\frac{1}{2},k+\frac{1}{2})} + \\ E^{n+\frac{1}{2}}_{y(i-\frac{1}{2},j+1,k+\frac{1}{2})} - E^{n+\frac{1}{2}}_{y(i+\frac{1}{2},j+1,k+\frac{1}{2})} \end{pmatrix} \end{aligned} \tag{2.12f}$$

where the material property coefficients are given by

$$C_{a(i,j,k)} = \frac{1 - \frac{\sigma_{(i,j,k)}\Delta t}{2\epsilon_{(i,j,k)}}}{1 + \frac{\sigma_{(i,j,k)}\Delta t}{2\epsilon_{(i,j,k)}}}, \tag{2.13a}$$

$$C_{b(i,j,k)} = \frac{\frac{\Delta t}{\epsilon_{(i,j,k)}\Delta l}}{1 + \frac{\sigma_{(i,j,k)}\Delta t}{2\epsilon_{(i,j,k)}}}, \tag{2.13b}$$

$$D_{a(i,j,k)} = \frac{1 - \frac{\sigma^*_{(i,j,k)}\Delta t}{\mu_{(i,j,k)}}}{1 + \frac{\sigma^*_{(i,j,k)}\Delta t}{2\mu_{(i,j,k)}}} \text{ and} \tag{2.13c}$$

$$D_{b(i,j,k)} = \frac{\frac{\Delta t}{\mu_{(i,j,k)}\Delta l}}{1 + \frac{\sigma_{(i,j,k)}\Delta t}{2\mu_{(i,j,k)}}}, \tag{2.13d}$$

that define the permittivity, permeability, conductivity, and equivalent magnetic loss term at a given (i, j, k) location. Each scalar component of $\boldsymbol{E}$ and $\boldsymbol{H}$ will have its own C or D coefficient matrices.

2.3 Numerical Dispersion

Physical electronmagnetic waves will naturally experience dispersion due to boundary conditions or innate properties of the propagation medium, which means their phase velocity will vary with frequency. While the FDTD algorithm can model this dispersion, numerical waves within the FDTD will also experience non-physical dispersion effects due to the method's discretization in space and time. That is, even in a vacuum setting, the phase velocity of a simulated wave will vary as a function of spatial step size, time step size, propagation direction, and frequency. The analytical dispersion relation for a physical plane wave in free space is given by

$$\left(\frac{\omega}{c}\right)^2 = (k_x)^2 + (k_y)^2 + (k_z)^2, \tag{2.14}$$

and the numerical dispersion relation derived from the FDTD algorithm is given by

$$\left[\frac{1}{c\Delta t} sin(\frac{\omega \Delta t}{2})\right]^2 = \left[\frac{1}{\Delta x} sin(\frac{\tilde{k_x}\Delta x}{2})\right]^2 + \left[\frac{1}{\Delta y} sin(\frac{\tilde{k_y}\Delta y}{2})\right]^2 + \left[\frac{1}{\Delta z} sin(\frac{\tilde{k_z}\Delta z}{2})\right]^2. \tag{2.15}$$

Where $\tilde{\boldsymbol{k}}$ is the numerical wave vector related to its vector components by

$$\tilde{k_x} = \tilde{k} cos\phi sin\theta,\ \tilde{k_y} = \tilde{k} sin\phi sin\theta,\ \tilde{k_z} = \tilde{k} cos\theta, \tag{2.16}$$

where ϕ is the azimuthal sweep $0 \leq \phi \leq 2\pi$ and θ is the zenith sweep $0 \leq \theta \leq \pi$.

The effects of spatial and temporal step-size on dispersion in the FDTD algorithm can be demonstrated visually by numerically solving for $\tilde{k}$ and plotting the components of the refractive indices along different propagation directions. Such a plot is shown in Figure 2.2, where the spatial-step size is set to be arbitrarily small such that its dispersion effects are negligible. The ideal physical dispersion case is indicated by a dashed purple curve, which is simply a unit circle. The solid lines denote varying time-step sizes.

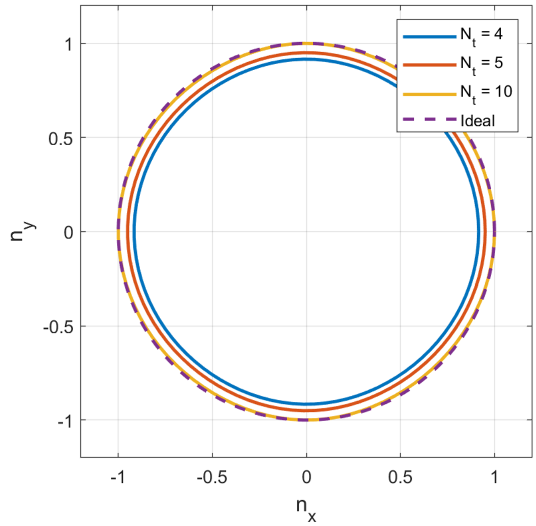

Figure 2.2: Refractive index components along the x and y axis showing isotropic dispersion. Time-step is selected by $\Delta t = \frac{1}{N_t f}$ Spatial-step is set to $\Delta l = \frac{\lambda}{10}$.

As Figure 2.2 indicates, the refractive index for a numerical wave is inversely proportional to the time-step size. That is to say, a larger time-step will lead to a numerical wave with a phase velocity greater than speed c.

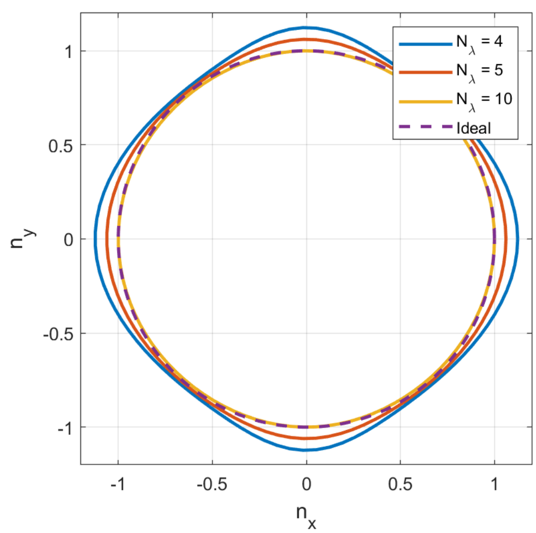

Figure 2.3: Phase portrait of the refractive index along the x and y axis showing anisotropic dispersion. Spatial-step is selected by$\Delta l = \frac{\lambda}{N_\lambda}$ Time-step is set to $\Delta t = \frac{1}{10f}$.

While the dispersive effects caused by the time-step size are isotropic, the dispersion due to spatial-step size will generate a numerical wave with anisotropic dispersion. Figure 2.3 shows that the numerical refractive index is furthest from unity along the major grid axes, and closest along the grid diagonals, which will distort the shape of a propagating wave. As the spatial and time steps decrease in size, the numerical wave propagation approaches the behavior of the ideal physical case. This can also be seen analytically by taking the limit of Equation 2.16 as Δx, Δy, Δz, and Δt approach zero, which will then reduce to the physical plane wave dispersion relation shown in Equation 2.14. From this analysis, it is made clear that selecting finer spatial-step and time-step sizes will lead to smaller errors that could result in nonphysical phenomena in a simulation.

2.4 Stability Conditions

As a consequence of the leap-frog time marching scheme used in the method, the FDTD algorithm has a stability criterion attached to it that couples time step size to spatial-step size. The update equations given in Equations 2.12 can be expressed as

$$\boldsymbol{h}^{n+1} = \boldsymbol{h}^{n} - \Delta t \boldsymbol{D}_e \boldsymbol{e}^{n+\frac{1}{2}} \tag{2.17a}$$

$$\text{and} \boldsymbol{e}^{n+\frac{1}{2}} = \boldsymbol{e}^{n-\frac{1}{2}} + \Delta t \boldsymbol{D}_h \boldsymbol{h}^{n+1}, \tag{2.17b}$$

where $\boldsymbol{h}$ is a vector containing all of the scalar magnetic field components, $\boldsymbol{e}$ is a vector containing all of the scalar electric field components, $\boldsymbol{D}_e$ is a matrix representing the discrete curl operation of the electric field $\frac{1}{\mu}\nabla_E\times$, and $\boldsymbol{D}_h$ is a matrix representing the discrete curl operation of the magnetic field $\frac{1}{\epsilon}\nabla_H\times$. By substituting Equation 2.17a into Equation 2.17b, the following is obtained:

$$\begin{bmatrix} \boldsymbol{h}^{n+1} \\ \boldsymbol{e}^{n+\frac{1}{2}} \end{bmatrix} = \begin{bmatrix} \boldsymbol{I} & -\Delta t \boldsymbol{D}_e \\ \Delta t \boldsymbol{D}_h & \boldsymbol{I} - \Delta t \boldsymbol{D}_h \boldsymbol{D}_e \end{bmatrix} \begin{bmatrix} \boldsymbol{h}^{n} \\ \boldsymbol{e}^{n-\frac{1}{2}} \end{bmatrix}. \tag{2.18}$$

By letting

$$U^n = \begin{bmatrix} \boldsymbol{h}^{n} \\ \boldsymbol{e}^{n-\frac{1}{2}} \end{bmatrix}, \tag{2.19}$$

and

$$\boldsymbol{G} = \begin{bmatrix} \boldsymbol{I} & -\Delta t \boldsymbol{D}_e \\ \Delta t \boldsymbol{D}_h & \boldsymbol{I} - \Delta t \boldsymbol{D}_h \boldsymbol{D}_e \end{bmatrix} \tag{2.20}$$

where $\boldsymbol{G}$ is typically referred to as an amplification factor. Equation 2.18 can then be written more simply as

$$U^{n+1} = \boldsymbol{G} U^n. \tag{2.21}$$

In order for stability to be achieved, the eigenvalues of $\boldsymbol{G}$ must be bounded by the unit circle of the complex plane, otherwise at each new time step n, the error will begin to grow exponentially. The eigenvalues of $\boldsymbol{G}$ can be found by the eigenvalue problem:

$$(\boldsymbol{G} - \boldsymbol{I})\boldsymbol{v} = (\lambda_G - 1)\boldsymbol{v} \tag{2.22}$$

where $\boldsymbol{v}$ are the eigenvectors of $\boldsymbol{G}$, and λ_G are the eigenvalues of $\boldsymbol{G}$. Plugging in Equation 2.20 for $\boldsymbol{G}$ then yields

$$\begin{pmatrix} 0 & -\Delta t \boldsymbol{D}_e \\ \Delta t \boldsymbol{D}_h & -\Delta t \boldsymbol{D}_h \boldsymbol{D}_e \end{pmatrix} \begin{pmatrix} \boldsymbol{v}_1 \\ \boldsymbol{v}_2 \end{pmatrix} = \Lambda_G \begin{pmatrix} \boldsymbol{v}_1 \\ \boldsymbol{v}_2 \end{pmatrix}, \tag{2.23}$$

where $\Lambda_G = (\lambda_G - 1)$. Letting $\boldsymbol{M} = \boldsymbol{D}_h \boldsymbol{D}_e$, Equation 2.23 can then be expressed as

$$-\Delta t \boldsymbol{D}_e \boldsymbol{v}_2 = \Lambda_G \boldsymbol{v}_1 \tag{2.24a}$$

$$\Delta t \boldsymbol{D}_h \boldsymbol{v}_1 - \Delta t \boldsymbol{M} \boldsymbol{v}_2 = \Lambda_G \boldsymbol{v}_2. \tag{2.24b}$$

Substituting Equation 2.24a into Equation 2.24b and multiplying by Λ_G then gives

$$\Lambda_G^2 \boldsymbol{v}_2 + \Delta t^2 \boldsymbol{M} \boldsymbol{v}_2 \Lambda_G + \Delta t^2 \boldsymbol{M} \boldsymbol{v}_2 = 0. \tag{2.25}$$

The discrete curl-curl operator matrix $\boldsymbol{M}$ is symmetric, and can be diagonalized such that

$$\boldsymbol{P}^{-1} \boldsymbol{M} \boldsymbol{P} = \boldsymbol{D}_m \tag{2.26}$$

where $\boldsymbol{P}$ is a projection matrix, and $\boldsymbol{D}_m$ is a diagonal matrix containing the eigenvalues λ_M of $\boldsymbol{M}$. Equation 2.25 then becomes

$$\boldsymbol{v}_2 (\boldsymbol{I} \Lambda_G^2 + \boldsymbol{D}_m \Delta t^2 \Lambda_G + \boldsymbol{D}_m \Delta t^2) = 0. \tag{2.27}$$

In order for Equation 2.27 to be true,

$$\Lambda_G^2 + \lambda_M \Delta t^2 \Lambda_G + \lambda_M \Delta t^2 = 0 \tag{2.28}$$

must also be true. Solving for the roots of Equation 2.28 then yields

$$\Lambda_G = \frac{-\lambda_M \Delta t^2 \pm \sqrt{(\lambda_M \Delta t^2)^2 - 4(\lambda_M \Delta t^2)}}{2}. \tag{2.29}$$

The eigenvalues of $\boldsymbol{G}$ are then found to be

$$\lambda_G = 1 - \frac{\lambda_M \Delta t^2 \pm \sqrt{(\lambda_M \Delta t^2)^2 - 4(\lambda_M \Delta t^2)}}{2}. \tag{2.30}$$

To meet the stability condition $|\lambda_G| \leq 1$, from Equation 2.30

$$\Delta t^2 \lambda_M \leq 4. \tag{2.31}$$

The maximum eigenvalues of $\boldsymbol{M}$ is found to be bounded by the relation

$$\lambda_M \leq 4 \left(\frac{1}{\Delta x^2} + \frac{1}{\Delta y^2} + \frac{1}{\Delta z^2} \right) \tag{2.32}$$

and when applied to Equation 2.31, we at last arrive at the stability condition

$$\Delta t < \frac{1}{c} \frac{1}{\sqrt{\frac{1}{\Delta x^2} + \frac{1}{\Delta y^2} + \frac{1}{\Delta z^2}}}. \tag{2.33}$$

This matches the result from [26] and is referred to as the Courant-Fredrichs-Lewy stability limit, or CFL condition for short.

With the dispersion results shown in the previous section and this stability condition in mind, the selection process for step-sizes generally begins by choosing a spatial-step size that is the minimum value between the smallest physical feature needed to be resolved, and $\Delta l = \frac{\lambda}{10}$, where λ is the wavelength corresponding to the highest frequency expected in the simulation. From here, the CFL condition is applied to select a step size

$$\Delta t = \frac{1}{c} \frac{CFLN}{\sqrt{\frac{1}{\Delta x^2} + \frac{1}{\Delta y^2} + \frac{1}{\Delta z^2}}} \tag{2.34}$$

where $CFLN < 1$, but selected to be close to unity, e.g. $CFLN = 0.999$.

2.5 Lumped Components

In general, lumped components can be modeled in FDTD by placing the component on an electric grid edge, and expressing it through Ampere's law as

$$\frac{\partial}{\partial t}\epsilon \iint \overrightarrow{E} \cdot d\overrightarrow{s} = \oint \overrightarrow{H} \cdot d\overrightarrow{l} - \iint \overrightarrow{J} \cdot d\overrightarrow{s}, \tag{2.35}$$

where

$$I = \iint \overrightarrow{J} \cdot d\overrightarrow{s}. \tag{2.36}$$

Any closed-form I-V can be applied to Equation 2.36 which can then be discretized and applied to the discrete form of Ampere's Law as in Equations 2.12 to generate an update equation that takes into account a lumped component. For example, a capacitor's I-V relationship is given by

$$I = C\frac{dV}{dt}, \tag{2.37}$$

if we place this capacitor upon an Ez grid ege, $\frac{dV}{dt}$ can be discretized and approximated as

$$V^n = \Delta z E^n_{z_{i,j,k+\frac{1}{2}}}. \tag{2.38}$$

Central difference approximations can then be applied $I = C\frac{dV}{dt}$, which yields

$$I^n = C\frac{\Delta z}{\Delta t}\left(E^{n+\frac{1}{2}}_{z_{i,j,k+\frac{1}{2}}} - E^{n\frac{1}{2}}_{z_{i,j,k+\frac{1}{2}}}\right). \tag{2.39}$$

This is then combined with with the appropriate equation from Equations 2.12, giving an update equation for a static capacitive lumped load

$$E_{z_{i,j,k+\frac{1}{2}}}^{n+\frac{1}{2}} = E_{z_{i,j,k+\frac{1}{2}}}^{n-\frac{1}{2}} + \frac{\Delta t}{\epsilon + C\frac{\Delta z}{\Delta x \Delta y}} \left[\left(\frac{H_{y_{i+\frac{1}{2},j,k+\frac{1}{2}}}^{n} - H_{y_{i-\frac{1}{2},j,k+\frac{1}{2}}}^{n}}{\Delta x} \right) - \left(\frac{H_{x_{i,j+\frac{1}{2},k+\frac{1}{2}}}^{n} - H_{y_{i,j-\frac{1}{2},k+\frac{1}{2}}}^{n}}{\Delta x} \right) \right]. \tag{2.40}$$

Similar processes can be followed to build update equations for resistors, inductors, or a combination of basic components. In Chapter 3, this method will be expanded upon to create an update equation for a time-varying capacitor.

2.6 Boundary Conditions

In practice, field component arrays are initialized to zero in an FDTD algorithm, and it is common for simulation domains to begin and end on $\boldsymbol{E}$ field components. This then means that at the boundary, $\boldsymbol{E}$ field components can't be updated as they lack adequate $\boldsymbol{H}$ field information.

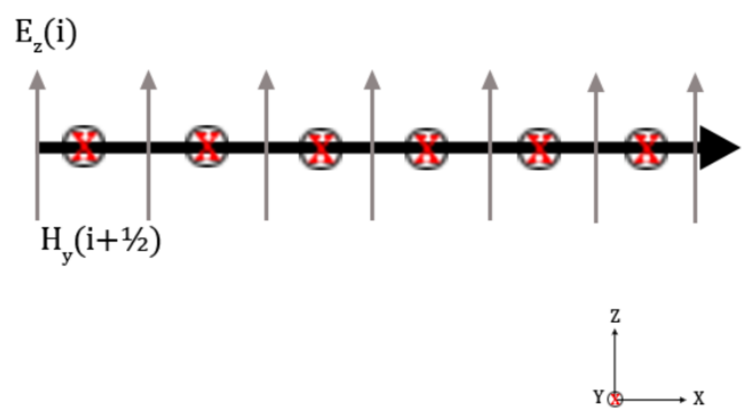

Figure 2.4: 1-D FDTD grid with the edge Ez component labeled.

Consider the simple 1-D case shown in Figure 2.4, the E_z update equation from Equations 2.12 reduces down to

$$E_{z(i)}^{n+\frac{1}{2}} = C_{az(i)} E_{z(i)}^{n-\frac{1}{2}} + C_{bz(i)} (H_{y(i+\frac{1}{2})}^{n} - H_{y(i-\frac{1}{2})}^{n}). \tag{2.41}$$

Because there is no H_y component at index $i - \frac{1}{2}$, $E_z(i)$ cannot be computed. Therefore the $\boldsymbol{E}$ field components at the boundaries of the simulation space are always zero, and will appear as a perfect electric conductor (PEC) to propagating waves. This will lead to reflections at the boundaries of the simulation space, which is problematic for cases requiring unbounded regions to represented. To minimize unwanted reflections, an absorbing boundary condition (ABC) is applied to the outer boundaries of the simulation. Early implementations of ABC's were computationally expensive, utilizing Green's functions to estimate the fields at the boundary from equivalent current densities [27]. A more efficient ABC has been implemented in the form of the perfectly matched layer (PML)[28], which acts as an absorbing medium analogous to the material found in anechoic chambers.

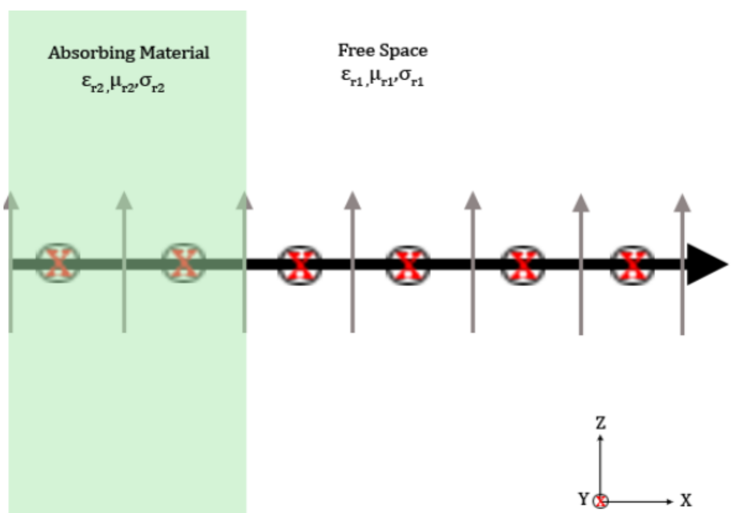

Figure 2.5: 1-D FDTD grid with the edge Ez component labeled.

The PML is implemented as a material that satisfies two conditions: (1) no reflections at the interface between free space and the absorbing medium, and (2) the propagating wave must be attenuated as it travels throughout the absorbing medium. Condition (1) requires that

$$\Gamma = \frac{\eta_2 - \eta_1}{\eta_1 + \eta_1} = 0, \tag{2.42}$$

where η_1 is the impedance of free space given by

$$\eta_1 = \sqrt{\frac{\mu_0}{\epsilon_0}}, \tag{2.43}$$

and η_2 is the impedance of a general medium [29] given by

$$\eta_2 = \sqrt{\frac{\mu_2\left(1 - j\frac{\sigma_2^*}{\omega_2\epsilon_2}\right)}{\epsilon_2\left(1 - j\frac{\sigma_2}{\omega_2\epsilon_2}\right)}}. \tag{2.44}$$

For condition (1) to hold,

$$\epsilon_2 = \epsilon_1, \tag{2.45a}$$

$$\mu_2 = \mu_1 \text{ and} \tag{2.45b}$$

$$\frac{\left(1 - j\frac{\sigma_2^*}{\omega_2\epsilon_2}\right)}{\left(1 - j\frac{\sigma_2}{\omega_2\epsilon_2}\right)} = 1. \tag{2.45c}$$

Applying these conditions yields a relation for the equivalent magnetic loss term,

$$\sigma^* = \sigma\left(\frac{\mu_0}{\epsilon_0}\right). \tag{2.46}$$

To satisfy condition (2), the conductive loss term σ must gradually increase from zero to a maximum value. This thesis implements a polynomial grading profile for σ, given by

$$\sigma(l) = \left(\frac{l}{d}\right)^m \sigma_{max} \tag{2.47}$$

where l is the distance into the absorbing material from the interface with free space, d is the physical thickness of the absorbing material, m is a polynomial grading coefficient, and

σ_{max} is the maximum conductivity of the material given by

$$\sigma_{max} = \frac{0.8\,(m+1)}{\eta_0 \Delta_l \sqrt{\epsilon_r \mu_r}} \tag{2.48}$$

and Δ_l is the spatial step size of the grid.

In the simulations presented in Chapters 3 and 4, OU-FDTD utilizes a PML with 10-cell thickness, and a grading coefficient of $m = 3$.

2.7 Conclusions

This chapter laid out the basic formulation of the FDTD method used to construct the OU-FDTD solver this thesis based its work on. Dispersion and stability considerations for spatial and time-steps sizes were discussed, and a method for adding lumped circuit components was presented. In Chapter 3, the section on lumped components will be expanded upon to include specific examples for time-varying components. In Chapter 4, dispersion caused by a physical medium is modeled, requiring the general form of the constitutive relations as shown in Equation 2.2, which will lead to a modification in the update equation for electric fields.

Chapter 3

Time-Varying Antenna Loads

This chapter will describe how time-varying loads can be implemented in FDTD through direct implementation as a lumped component, and through co-simulation with SPICE. A dipole loaded with a switch is considered, as well as a number of square loop antennas loaded with time-varying capacitors. The ability of two commercial solvers, XFDTD[9] and CST Studio[8], to model time-variant behavior will also be briefly discussed. A frequency domain solver, CMMoM [10] is used to generate parametric amplification designs for the implementation of time-varying capacitor loads. Generally, a time-varying component will introduce harmonics in the simulation space shown by the relation

$$f_h = f_0 \pm n f_p, \tag{3.1}$$

where f_h is the harmonic frequency observed, f_0 is the excitation frequency, and n is a positive integer. This will necessitate a smaller spatial step to accurately resolve the smaller wavelengths, and consequently a smaller time step size to satisfy the stability condition given in Chapter 2.

3.1 Time-Varying Components in FDTD

3.1.1 Switched Loads

In the FDTD method, a switch load can be implemented by applying a transform to the electric field of the grid-cell containing the load represented by

$$E^n_{i,j,k} = E^n_{i,j,k} S^n \tag{3.2}$$

where i, j, k are the indices denoting the location of the switch load, and S^n denotes the state of the switch at timestep n. This transform is applied after the typical electric field update equation. Physically, when the switch is closed ($S^n = 0$), $E^n_{i,j,k} = 0$, which means that a propagating electric field sees the closed switch as a perfect electric conductor. When the switch is open, $E^n_{i,j,k}$ is determined by the material properties present at that grid-cell location. The switch's waveform can be represented by any waveform, but modifications must be made to ensure simulation accuracy is maintained. For example, in a square wave the discontinuity caused by the instantaneous transition from an "on" to "off" state in the switch can be remedied by adding a transition period in between switch states, which is implemented as a linear ramp-up or ramp-down. In this work, a transition period equal to 60 timesteps was used in test cases. This nets a signal that is still mostly square as seen in Fig. 3.1 without introducing any high-frequency transients.

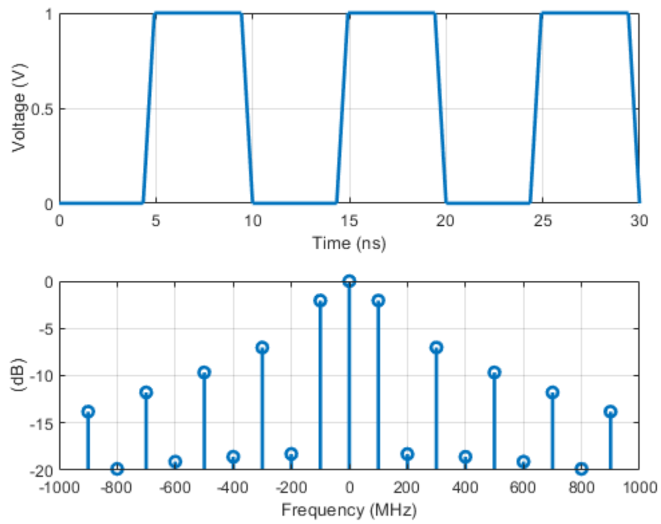

Figure 3.1: 100MHz switch waveform with a transition period in the time-domain(top) and frequency-domain(bottom)

3.1.2 Simulation of Switched Loads

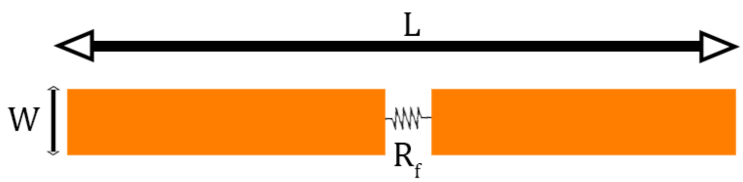

Figure 3.2: Ribbon dipole antenna. $R_F = 50\Omega$, $D = 15cm$, $W = 0.5cm$ with a plane wave excitation of 100MHz. $d = 208mm \approx \frac{\lambda}{14}$.

The half-wave ribbon dipole shown in Figure 3.2 was simulated in OU-FDTD with a switch loaded across its feed point. The switch waveform is given in Figure 3.1.

A comparison between the 60 time step transition and a single time step transition is shown in Figure 3.3 to demonstrate the need for transition time between states. Using a switch transition that takes place over a single time step introduces a spike into the signal as the switch transitions from an open to a closed state. Additionally, the frequency spectrum shows high frequency content at higher magnitudes.

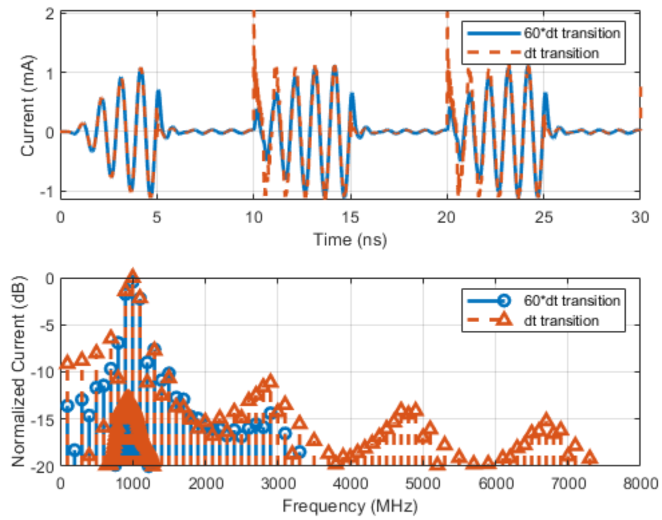

Figure 3.3: Time and frequency domain currents across the resistor representing the dipole feed for a switch loaded dipole with switch transition times of 1 timestep and 60 timesteps.

A commercial solver was desired to assist in validation, for which XFDTD was the first option explore. This software has limited support for investigating antennas loaded with time-varying components. It contains a built in ”Switch” that allows users to define a waveform as a table of state transitions. The same half-wave dipole with a switch load was simulated in XFDTD, and its results compared to those obtained in OU-FDTD. From Figure 3.4 at the excitation frequency, the results between OU-FDTD and XFDTD show agreement with 0.1 dB. The harmonics show agreement within 1 dB of each other as well, with the exception of the harmonic at 1500 MHz, where the difference is 2.5 dB.

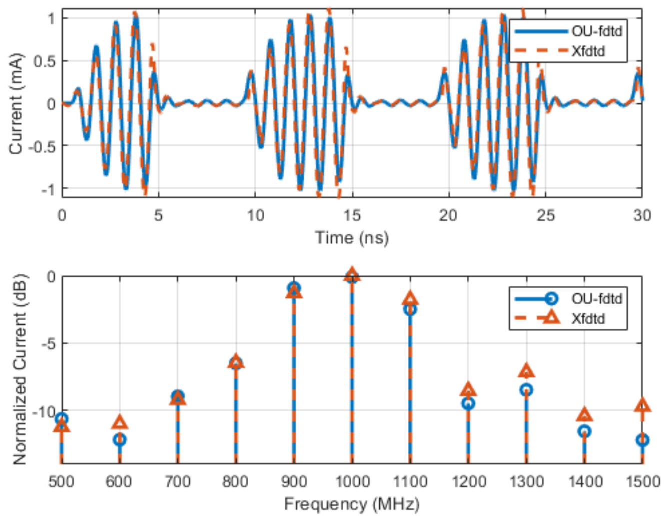

Figure 3.4: Time and frequency domain currents at the feed for a switch loaded dipole. Incident plane wave at 1GHz and switching frequency of 100MHz. Simulated in OU-FDTD and XFDTD.

3.1.3 Time-Varying Capacitive Load

An RF switch load is effectively a time-varying resistance, which will naturally add ohmic loss to the antenna aperture. The time-varying capacitance implemented in this section offers a way to introduce time-variance without adding a real impedance. The process for a time-varying capacitor is very similar to the case of a lumped static-capacitor shown in Equation 2.40, except the I-V relationship must be modified to account for the changing capacitance. For a time-varying capacitor, this is given by

$$I = \frac{d}{dt}Q = \frac{d}{dt}[CV] \text{ and } I = C\frac{dV}{dt} + V\frac{dC}{dt}. \tag{3.3}$$

After discretization, C^n and V^n must be time-averaged to place them on the correct temporal grid. This gives

$$
\begin{aligned}
I^n = &\left(\frac{C^{n+\frac{1}{2}} + C^{n-\frac{1}{2}}}{2}\right)\left(\frac{V^{n+\frac{1}{2}} - V^{n-\frac{1}{2}}}{\Delta t}\right) \\
&+ \left(\frac{V^{n+\frac{1}{2}} + V^{n-\frac{1}{2}}}{2}\right)\left(\frac{C^{n+\frac{1}{2}} - C^{n-\frac{1}{2}}}{\Delta t}\right),
\end{aligned} \tag{3.4}
$$

which when combined with the discrete form of Ampere's Law will give the electric field update equation

$$
\begin{aligned}
E_{z_{i,j,k+\frac{1}{2}}}^{n+\frac{1}{2}} = &Ca_1 E_{z_{i,j,k+\frac{1}{2}}}^{n-\frac{1}{2}} \\
&+ Ca_2\left[\left(\frac{H_{y_{i+\frac{1}{2},j,k+\frac{1}{2}}}^{n} - H_{y_{i-\frac{1}{2},j,k+\frac{1}{2}}}^{n}}{\Delta x}\right) - \left(\frac{H_{x_{i,j+\frac{1}{2},k+\frac{1}{2}}}^{n} - H_{y_{i,j-\frac{1}{2},k+\frac{1}{2}}}^{n}}{\Delta x}\right)\right],
\end{aligned} \tag{3.5}
$$

where C_{a1} and C_{a2} are coefficients given by

$$
Ca_1 = \frac{\epsilon \Delta x \Delta y + \Delta z C^{n-\frac{1}{2}}}{\epsilon \Delta x \Delta y + \Delta z C^{n+\frac{1}{2}}} \text{ and} \tag{3.6a}
$$

$$
Ca_2 = \frac{\Delta t}{\epsilon \Delta x \Delta y + \Delta z C^{n+\frac{1}{2}}}. \tag{3.6b}
$$

C^n is implemented as

$$
C^n = C_0\left(1 + \gamma sin(2\pi f_p t^n + \phi)\right), \tag{3.7}
$$

where C_0 is a DC capacitance, γ is a modulation factor, f_p is a pumping frequency, t^n is the time at step n, and ϕ is some phase shift.

3.1.4 Simulation of Time-Varying Capacitive Loads

The time-varying capacitor model given in the previous section was used to simulate several antennas designed using CM-MoM. Again, a commercial solver was also desired for validation. Remcom's XFDTD was unable to support time-varying capacitors. While it also advertises SPICE co-simulation support, it only allows a limited variety of basic SPICE components to be used, making it impossible to even approximate a time-varying capacitor. Simulia Corp's CST Studio was looked at as an alternative. CST utilizes the Finite-Integration Technique (FIT), which when used with a cartesian spatial discretization and leap-frog time stepping scheme, reduces down to the FDTD method [30]. While CST also lacks a direction implementation of time-varying components, it does have full SPICE support, which allows for an equivalent time-varying capacitor model [31] to be implemented as a SPICE component. In the cosimulation method, current is calculated at the electric field component containing the SPICE component. This current is passed into the SPICE simulation as a current source and the circuit is solved numerically. The voltage across the circuit is then calculated, and passed back into the FDTD simulation. The voltage is then converted into an equivalent electric field with the approximation given in Equation 2.38, which is used in subsequent H field updates. This process is repeated at every time step.

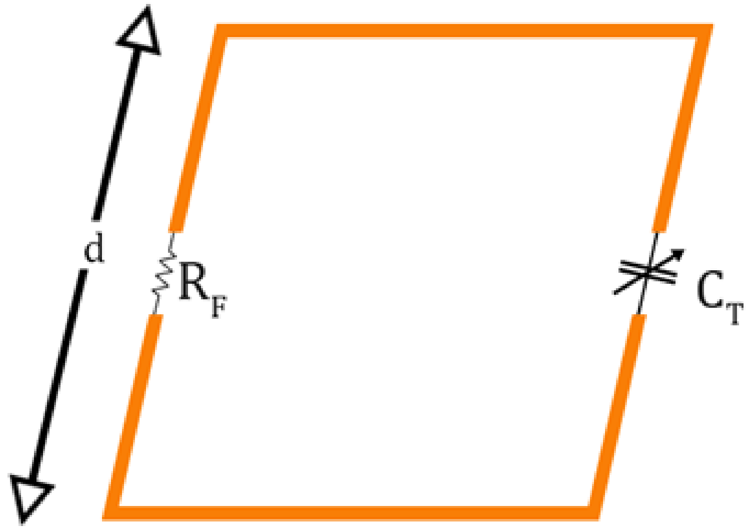

Figure 3.5: Loop Antenna. $R_F = 26\Omega$, $C_0 = 2.7pF$, $\gamma = 0.6$, f_p = 195MHz, $\phi = 0$, with a plane wave excitation of 100MHz. $d = 208mm \approx \frac{\lambda}{14}$.

A comparison between CST, OU-FDTD, and CM-MoM was run for the antenna configuration shown in Figure 3.5. While the physical models for CST and OU-FDTD were very similar - planar square loops - in this case the impedance matrix for CM-MoM was pulled from a wire segment model generated in Altair's Feko. Additionally, while OU-FDTD uses a uniform grid mesh, CST Studio makes use of an adaptive meshing technique, where the grid cell meshing is finer near areas of interest (e.g., at the feed and load) to more accurately resolve the fields at those locations. Figure 3.6, plots the time-domain currents across the feed resistor. For the results from CM-MoM, this data was calculated via an inverse fourier transform of the frequency domain results at the port representing the antenna feed. The results from the time-domain solvers are truncated to the first period when steady-state is reached. As the figure shows, once this condition is met the solvers show excellent agreement with each other.

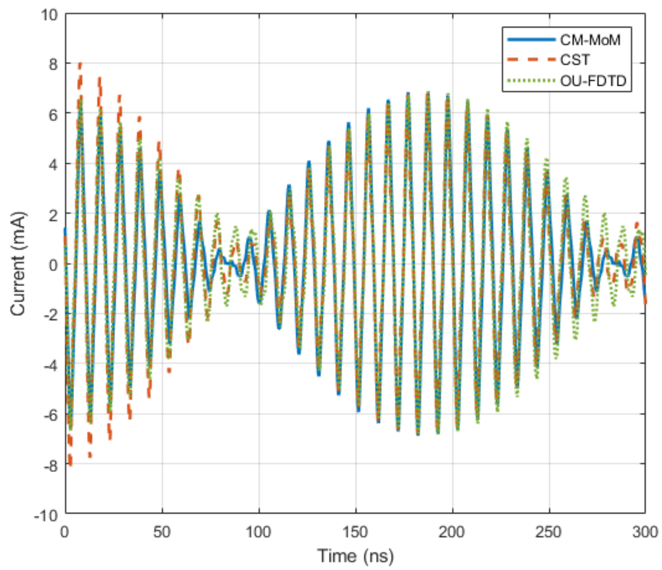

Figure 3.6: Time domain current across the feed resistor (R_F in Figure 3.5). Simulated in CM-MoM, CST Studio, and OU-FDTD. Truncated to first steady-state period.

When the excitation frequency and first difference harmonic are relatively close (≈ 10 MHz or less), the simulation must be run for an adequate amount of time to resolve the resulting beat frequency and allow it to reach steady state. Figure 3.7 demonstrates this phenomena for a simulation running at a 97 MHz excitation frequency with a 200 MHz pumping frequency. This creates a difference harmonic at 103 MHz, which leads to a beat frequency of 6 MHz. This beat has a period of ≈ 0.1667 μs. Even with this relatively short period, the simulation must run out to around beyond 7 μs to reach steady state.

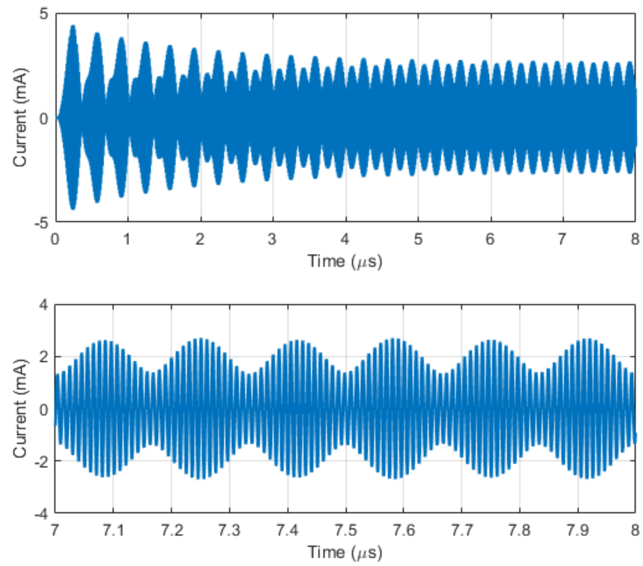

Figure 3.7: Time domain results showing a 6MHz beat frequency.

In the next test case, the impedance matrix for CM-MoM was extracted from the Antenna Toolbox for MATLAB (AToM) [32]. This allowed for the antenna geometries between CST and CM-MoM to be nearly identical, as AToM is able to generate a planar loop similar to CST.

R_F	C_0	γ	f_p	ϕ	f_{ex}	d
6Ω	4.0pF	0.05	200MHz	0	100MHz	150mm

Table 3.1: Design parameters for the first time-varying capacitor antenna design.

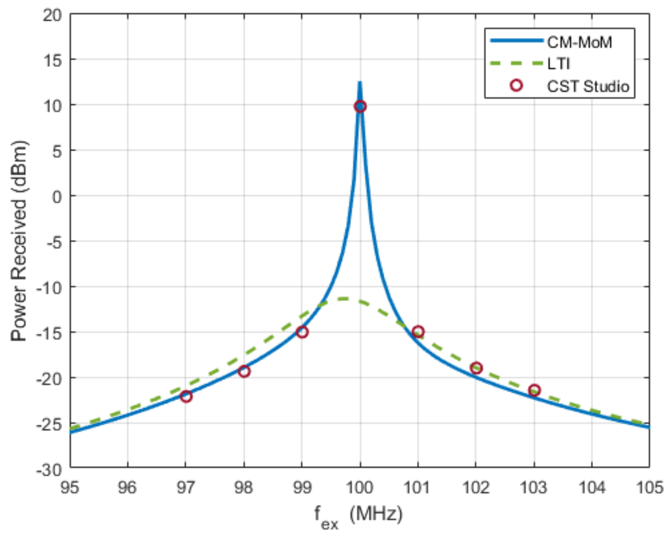

Figure 3.8: Power received over an excitation frequency sweep for the first time time-varying capacitor antenna design. LTI comparison is a conjugate match with $R_F = 6$ and $C_0 = 4.0pF$.

For this design, time-domain simulations were run at multiple excitation frequencies to see how they compared with excitation the sweep of CM-MoM for the same design. As this comparison would require several simulations of the same design, CST-Studio was used in place of OU-FDTD. At the time, CST Studio was capable of completing simulations much faster than OU-FDTD due to its adaptive meshing and parallel processing capability. The degenerate mode design has a narrow bandwidth high peak at 100 MHz. The design shows ≈ 24 dB of gain over the ideal LTI case for a loop antenna of this size, with a narrower 3 dB bandwidth. There is approximately a 2.7 dB difference of gain between CST and CM-MoM at the peak. Designs with narrow bandwidth were found to be sensitive to small changes in the design parameters or underlying antenna models. In this case, the location of the first series resonance at 100 MHz was shifted to the right 120 kHz in CST, which is reflected in the shifted curve for CST in Figure 3.8. This difference largely arises from the different loading methods between CM-MoM and finite-difference or finite-integration techniques. In FDTD and FIT, a physical gap is modeled where the load is placed that introduces fringing field effects. CM-MoM does not model a physical gap at load locations;

instead, a submatrix representing the impedance of the load is added to the appropriate port location of the antenna's impedance matrix.

R_F	C_0	γ	f_p	ϕ	f_{ex}	d
1Ω	4.076pF	0.222	492MHz	0	100MHz	150mm

Table 3.2: Design parameters for the second time-varying capacitor antenna design.

A design for an upconverting amplifier was explored using parameter sweeps in CM-MoM, using the same loop configuration shown in Figure 3.5 with the parameters listed in Table 3.2. In an upconverting amplifier design, one would expect to see significant gain over the excitation frequency at the first sum harmonic. In CM-MoM, the design shows amplification at both the excitation frequency and the first sum harmonic. However, the design was also unable to be verified in time-domain solvers. Figure 3.9 plots the power received at a sweep of the excitation frequency, and power received across the subsequent first sum harmonics. While CST Studio and OU-FDTD showed amplification at the excitation frequency, there was no amplification at the sum harmonic. This is likely due to a tuning discrepancy between the two solver methods. As discussed above, loading is handled differently between the time-domain solvers and CM-MoM, which leads to minor differences in the frequency location of their resonances. As this design has an even narrower bandwidth than the degenerate mode design shown in Figure 3.8, it requires even more precise tuning to the correct resonance.

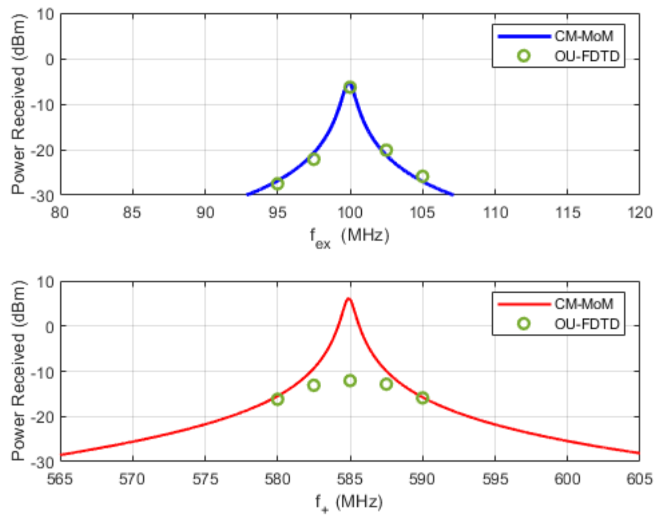

Figure 3.9: Power received around the excitation frequency(top) and the first sum harmonic (bottom) for the upconversion design listed in Table 3.2

Finally, the impacts of parametric amplification on a modulation scheme was investigated. The design's parameters are given in Table 3.3, this time however the plane, wave excitation was modulated with an on-off key scheme, shown in Figure 3.10. On-off keying is a very simple amplitude modulation scheme, wherein the presence of the carrier wave denotes a binary one, and its absence denotes a binary zero.

R_F	C_0	γ	f_p	ϕ	f_{ex}	d
50Ω	3.65pF	0.542	200MHz	0	100MHz	208mm

Table 3.3: Design parameters for the third time-varying capacitor antenna design.

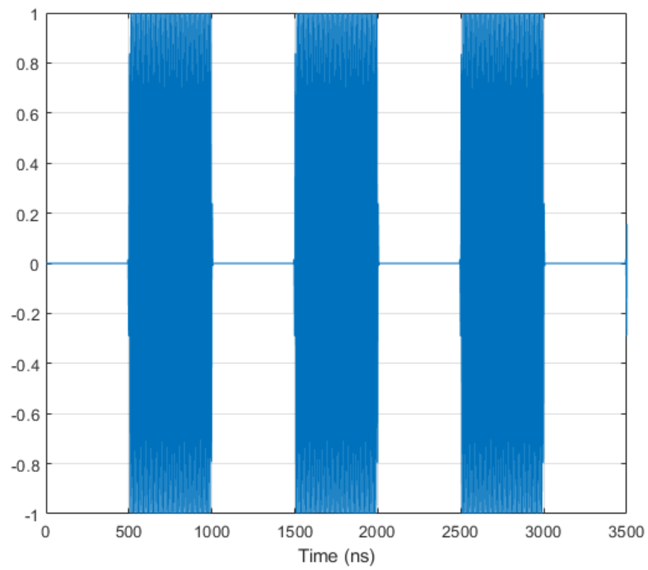

Figure 3.10: On-off key modulation scheme. Pulse width of 500ns.

Figure 3.11 plots the current across the feed resistor for the non-LTI antenna design and an LTI antenna design of the same geometry (square planar loop), loaded to achieve a conjugate match. The non-LTI antenna signal has a much higher amplitude, but also experiences significant distortion compared to the LTI antenna. For most of the duration of the "on" state, it is ramping up to, but not reaching, maximum amplification. In the "off" state, the current across the resistor does not full dissipate before the next transition occurs.

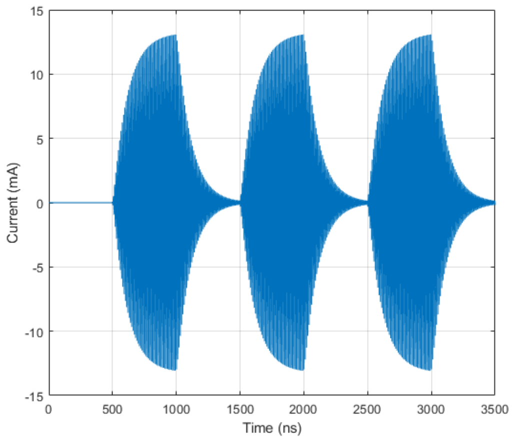

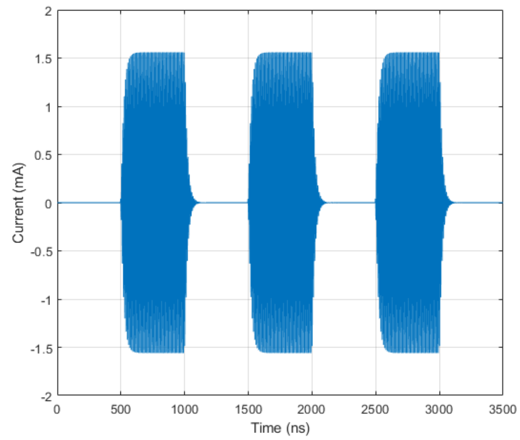

((a)) **((b))**

Figure 3.11: Time domain current across the feed resistor (R_F in Figure 3.5). (a) Non-LTI antenna design, and (b) LTI antenna design. Simulated in CST Studio.

3.2 Discussion

In general, commercial full wave time-domain solvers are currently lagging behind the needs of researchers investigating non-LTI antenna phenomena. XFDTD can effectively duplicate a time-varying resistor with their switch component, but time-varying reactances are not possible at this time due to component limitations in their SPICE co-simulation. CST Studio has full SPICE integration, which allows for various time-varying components to be simulated via co-simulation. However, it lacks a direct implementation of time-varying components such as what is shown in Equation 3.7.

This chapter also revealed a general weakness of the FDTD method, which is the steady-state analysis of highly resonant structures. Antennas with a narrow bandwidth – and consequently high Q – have transient responses that requires computation of long time sequences to resolve. These antenna structures also required small spatial step sizes relative to the simulated wavelength, which due to the CFL stability criterion lead to a time step that was much smaller than what would be required by accuracy. The combination of long time sequences and small time steps created excessive simulation runtimes. In CST Studio, which was far more efficient than OU-FDTD at the time, the simulation of a single design could take as long as 18 hours to complete. By comparison, CM-MoM is capable of iterating through thousands of design parameter combinations in the same amount of time. It is however, incapable of simulating transient behaviors, such as what was shown in the on-off key example. In this way, the two solver methods can be used to complement one another. Initial designs can be generated via the fast parameter sweeps of CM-MoM, which can then be recreated in FDTD for transient analysis. Non-LTI antenna designs that are highly sensitive to the frequency location of resonances, such as the upconverter design from Table 3.2, will require more care to ensure the antenna models between the two solver techniques closely align. For example, the effects of the physical gaps at the feed and load in FDTD and FIT will need to be modeled and accounted for.

Chapter 4

Modeling the Human Head at Radio Frequencies

This chapter provides analysis on the interaction of a plane wave excited by linear frequency modulated waveforms with the human head. The analysis is carried out with two time-domain solvers, OU-FDTD and Remcom's XFDTD. Similar research typically looks at SAR values, calculated in accordance with the IEEE standard as

$$SAR = \frac{\sigma |\boldsymbol{E}|^2}{\rho}, \tag{4.1}$$

where σ is the electrical conductivity of the material, ρ is the mass density of the material, and $\boldsymbol{E}$ is the steady-state or time-averaged magnitude of the electric field [33]. While this is a useful metric for gauging human safety standards, the time-averaging or steady-state requirement may smooth out interesting peaks in the time domain. In this work, SAR is not calculated, and results are instead left in the form of electric field magnitudes over time.

4.1 Dispersive Material Modeling

The dielectric behavior of human tissue is frequency dependent, which means that the simplified constitutive relation for $\boldsymbol{E}$ and $\boldsymbol{D}$ such as in Equation 2.3 cannot be used. Instead, the relationship between the $\boldsymbol{E}$ and $\boldsymbol{D}$ is given as

$$\boldsymbol{D}(t) = \epsilon(t) \circledast \boldsymbol{E}(t) \text{ or } \boldsymbol{D}(\omega) = \epsilon(\omega)\boldsymbol{E}(\omega). \tag{4.2}$$

Performing the convolution in the time-domain would require preserving the $\boldsymbol{E}$ field data at every time step for the entire simulation space, which would require unfeasible amounts of computer memory. Likewise, performing a fourier transform and inverse fourier transform at each iteration of the loop would be computationally inefficient. To solve this dilemma, relaxation models are used to describe the frequency dependent permittivity. XFDTD defaults to a four-term Cole-Cole model when a voxelized object is imported. OU-FDTD utilized a two-term Debye model, following the method used by Ireland and Abbosh [34]. The two-term Debye model is given by

$$\epsilon(\omega) = \epsilon_\infty + \frac{\Delta\epsilon_1}{1 + (j\omega\tau_1)} + \frac{\Delta\epsilon_2}{1 + (j\omega\tau_2)} + \frac{\sigma}{(j\omega\epsilon_0)}, \tag{4.3}$$

where ϵ_∞, $\Delta\epsilon_1$, $\Delta\epsilon_2$, τ_1, τ_2, and ω are fitting parameters. In the Cole-Cole model, the relaxation time term $(j\omega\tau_n)$ in the denominator is replaced with $(j\omega\tau_n)^{1-\alpha}$, where α is a "broadening" term that transforms the discrete relaxation time into a distribution of relaxation times. This leads to a more accurate representation of the frequency dependent permittivity, at the cost of increased computational complexity. The Debye parameters were fit to data primarily from the Gabriel & Gabriel database [15] across the frequency range 100MHz to 5GHz using a particle swarm optimization algorithm. Tissues not found in the Gabriel & Gabriel database were instead fit to data from the IT'IS Foundation database [35]. The generated Debye parameters used in this work are given in Table 4.1. Equation 4.3 is substituted into the constitutive relation between the displacement and electric field for linear, isotropic dispersions

$$\boldsymbol{D}(\omega) = \left[\epsilon_\infty + \frac{\Delta\epsilon_1}{1+(j\omega\tau_1)} + \frac{\Delta\epsilon_2}{1+(j\omega\tau_2)} + \frac{\sigma}{(j\omega\epsilon_0)}\right]\boldsymbol{E}(\omega), \tag{4.4}$$

which after applying an inverse fourier transform yields

$$\sigma\boldsymbol{E} + \gamma_1\frac{\partial\boldsymbol{E}}{\partial t} + \gamma_2\frac{\partial^2\boldsymbol{E}}{\partial t^2} + \gamma_3\frac{\partial^3\boldsymbol{E}}{\partial t^3} = \frac{\partial\boldsymbol{D}}{\partial t} + \gamma_4\frac{\partial^2\boldsymbol{D}}{\partial t^2} + \gamma_5\frac{\partial^3\boldsymbol{D}}{\partial t^3}. \tag{4.5}$$

Central difference approximations are be applied to Equation 4.5, which then nets an update equation for the electric field of the form

$$\begin{aligned}
E_z \mid_{i,j,k}^{n+1} =& \frac{1}{\gamma_1}\left(\frac{D_z \mid_{i,j,k}^{n+1} - D_z \mid_{i,j,k}^{n-2}}{3\Delta t}\right) \\
&+ \frac{\gamma_4}{\gamma_6}\left(\frac{D_z \mid_{i,j,k}^{n+1} - D_z \mid_{i,j,k}^{n} - D_z \mid_{i,j,k}^{n-1} + D_z \mid_{i,j,k}^{n-21}}{2\Delta t^2}\right) \\
&+ \frac{\gamma_5}{\gamma_6}\left(\frac{D_z \mid_{i,j,k}^{n+1} - 3D_z \mid_{i,j,k}^{n} + 3D_z \mid_{i,j,k}^{n-1} - D_z \mid_{i,j,k}^{n-21}}{\Delta t^3}\right) \\
&+ \frac{1}{\gamma_6}\left(\frac{\sigma}{16} + \frac{\gamma_1}{3\Delta t} - \frac{\gamma_2}{2\Delta t^2} + \frac{\gamma_3}{\Delta t^3}\right) E_z \mid_{i,j,k}^{n-2} \\
&+ \frac{1}{\gamma_6}\left(\frac{\gamma_2}{2\Delta t^2} - \frac{3\gamma_3}{\Delta t^3} - \frac{9\sigma}{16}\right) E_z \mid_{i,j,k}^{n-1} \\
&+ \frac{1}{\gamma_6}\left(\frac{\gamma_2}{2\Delta t^2} + \frac{3\gamma_3}{\Delta t^3} - \frac{9\sigma}{16}\right) E_z \mid_{i,j,k}^{n},
\end{aligned} \tag{4.6}$$

where

$$
\begin{aligned}
\gamma_1 &= \epsilon_0 \left(\Delta\epsilon_1 + \Delta\epsilon_2 + \epsilon_\infty\right) + \sigma\left(\tau_1 + \tau_2\right) \\
\gamma_2 &= \epsilon_0 \left(\Delta\epsilon_1 \tau_2 + \Delta\epsilon_2 \tau_1 + \epsilon_\infty \tau_1 + \epsilon_\infty \tau_2\right) + \sigma \tau_1 \tau_2 \\
\gamma_3 &= \epsilon_0 \epsilon_\infty \tau_1 \tau 2 \\
\gamma_4 &= \tau 1 + \tau 2 \\
\gamma_5 &= \tau 1 \tau 2 \\
\gamma_6 &= \left(\frac{\gamma_1}{3\Delta t} + \frac{\gamma_2}{2\Delta t^2} + \frac{\gamma_3}{\Delta t^3} - \frac{\sigma}{16}\right).
\end{aligned}
\tag{4.7}
$$

The displacement field D_z is found by a standard FDTD update equation derived from Ampere's Law [26]. Equation 4.6 and similar equations for E_x and E_z were implemented in OU-FDTD.

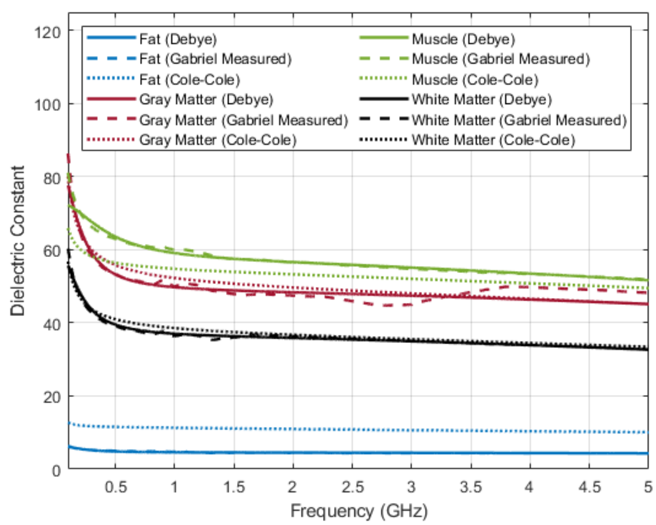

Figure 4.1: Modeled and measured effective dielectric constant for four different human tissues.

Figure 4.1 plots the dielectric constant of several different tissues across frequency for measured data, the two-term Debye used in OU-FDTD, and the four-term Cole-Cole model used in XFDTD. There are discrepancies between XFDTD's Cole-Cole model and OU-FDTD's Debye model in fat and muscle tissues. This was found to be caused by

XFDTD fitting to data from the IT'IS database by default, which in some cases differs from the measured profiles found in the Gabriel & Gabriel database. As variance in dielectric properties is to be expected between individuals, this discrepancy was left as-is to investigate its impact on simulated results. For the rest of the tissues used in this work, the modeled dielectric profiles showed agreement comparable to the results seen in Figure 4.1 for gray and white matter.

Table 4.1: Debye Parameters for Human Tissue (100MHz-5GHz)

Tissue Type	ϵ_∞	$\Delta\epsilon_1$	$\Delta\epsilon_2$	$\tau_1(ps)$	$\tau_2(ns)$	σ
Blood	10	44.6	24.7	10.8	1.16	1.53
Bone (Cancellous)	7.5	10.6	10.0	16.0	0.62	0.13
Bone (Cortical)	4.1	8.06	3.71	17.1	0.45	0.07
Brain (Gray Matter)	1	47.6	36.9	9.02	0.84	0.57
Brain (White Matter)	4.9	31.0	24.0	11.3	0.80	0.31
Cartilage	10	28.3	17.6	15.1	0.55	0.46
Cerebellum	10	38.5	60	11.2	1.43	0.55
Cerebrospinal Fluid	1	66.8	4.18	9.45	0.49	1.59
Dura	1	44.7	11.7	11.3	0.35	0.4
Eye (Cornea)	10	40.3	12.8	11.6	0.49	0.91
Eye (Lens)	7.0	42.0	7.98	10.2	0.26	0.59
Eye (Sclera)	10	43.0	13.1	11.9	0.56	0.86
Eye (Virtreous)	1	66.7	0.98	8.6	0.22	0.41
Fat (Not Infiltrated)	3.2	1.36	1.91	13.8	0.74	0.03
Gland	10	47.9	6.25	9.90	0.30	0.79
Intervertebral Disc	9.2	26.7	9.2	4.93	0.14	0.85
Muscle	10	46.9	16.2	11.4	0.38	0.79
Nerve	10	22.4	22.0	12.7	0.94	0.32
Salivary Gland	1.0	68.9	4.81	0.84	0.14	0.68
Skin	10	28.4	26.0	11.9	1.05	0.37

Two different human phantom models were used in this work: the high resolution multimodal imaging-based detailed anatomical (MIDA) model [36], and the Duke model from the Virtual Family population [37], both maintained by the IT'IS foundation. MIDA was acquired from scans of a 29-year old female from the head down to the C5 vertebrae in the neck. Duke is a full body model of a 34-year old male. While both models were acquired at a resolution of 0.5 mm, they were revoxelized at a resolution of 1 mm to increase computational efficiency. The Duke model was only simulated from the sternum and up for the same reason. Figure 4.2 is a side-by-side comparison of the models' interiors, which shows that the MIDA model offers more detail in terms of physical structures rendered. Of particular note is that the MIDA model fully details the ear canal and pharyngotympanic tube, while the Duke model effectively absorbs these structures into the surrounding muscle tissue. Additionally, MIDA has a significant amount of adipose tissue(purple) in the region between the ears. In the Duke model, this region is filled primarily with general muscle tissue(bright green).

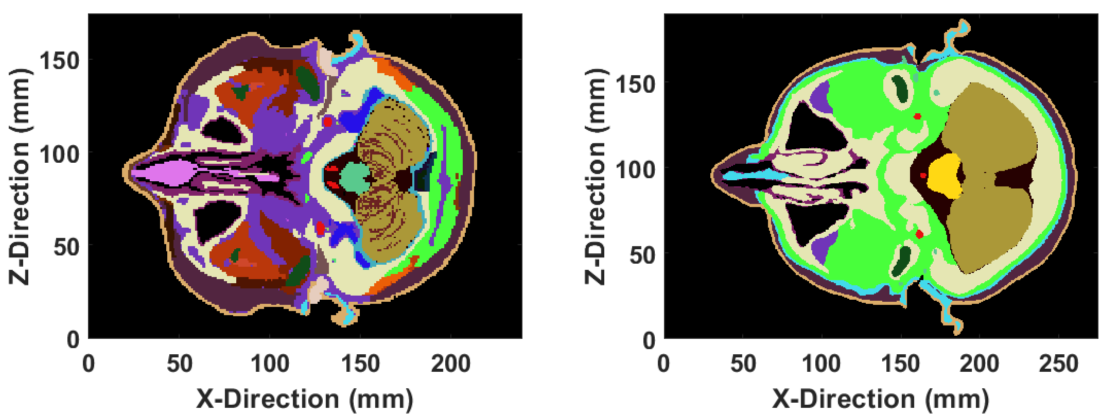

((a)) ((b))

Figure 4.2: Cut planes of the head phantoms coplanar with the ear canal. Color coded by unique tissue ID. (a) MIDA model. (b) Duke model.

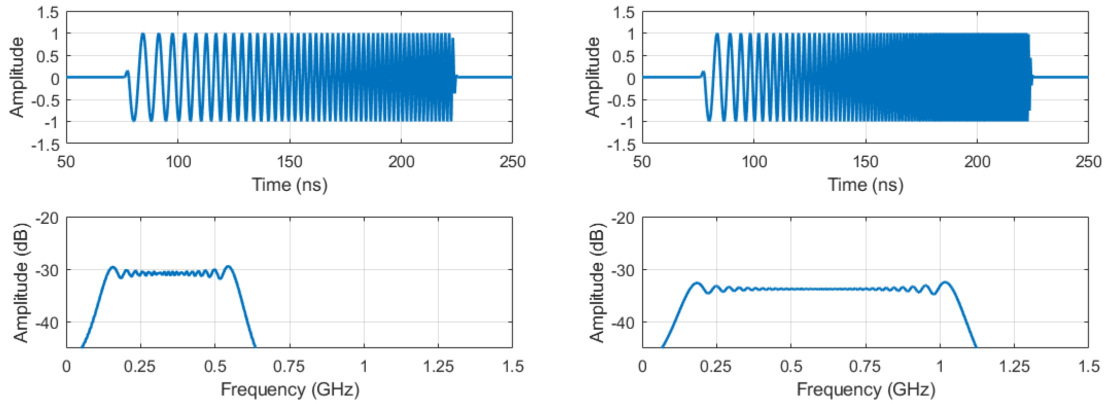

((a)) ((b))

Figure 4.3: Time and frequency domain representations of the LFM waveforms used in this work. (a) LFM1: $\beta = 400$MHz, $\tau = 150$ns. (b) LFM2: $\beta = 840$MHz, $\tau = 150$ns.

To investigate the frequency dependent properties of the tissue models, linear-frequency modulated (LFM) waveforms were injected as plane waves into the simulation space. The frequency range for LFM1 shown in Figure 4.3(a) was chosen arbitrarily. The frequency range for the LFM2 shown in Figure 4.3(b) was after initial simulations with LFM1 produced a notable phenomena requiring higher frequencies for further investigation. The simulations were performed with a plane wave propagating towards the side of the 3D human models, with the electric field polarized along the height axis of the models.

4.2 Simulation Results

Results in this work are given as electric field amplitudes normalized to the maximum amplitude of the plane wave excitation.

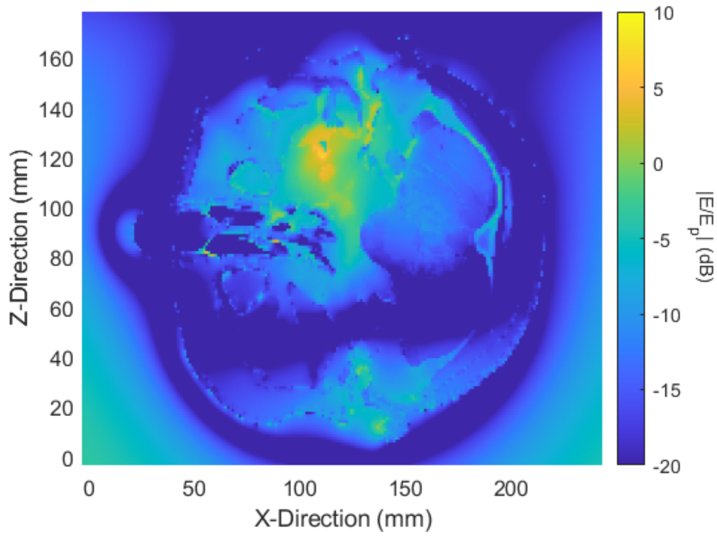

Figure 4.4: Electric field amplitude relative to the incident plane wave(LFM1) within the MIDA model simulated in OU-FDTD. Cross-sectional view(coplanar with the ear canal) shown at peak amplitude.

Initial simulations with LFM1 revealed electric field amplitudes exceeding those of the incident plane wave. These high field strengths are focused in the middle of the head, primarily in adipose and cortical bone tissue. The notable exception to this being the ear canal and pharyngotympanic tube, which also experience greater than unity normalized field strengths. While this effect is most prevalent on the side of the head upon which the plane wave is incident, normalized field amplitudes approaching unity do still appear in the opposite ear canal and some of the surrounding cortical bone and fat tissue. This effect was not seen within the brainstem or cerebellum, nor anywhere throughout the brain as shown in Figure 4.5.

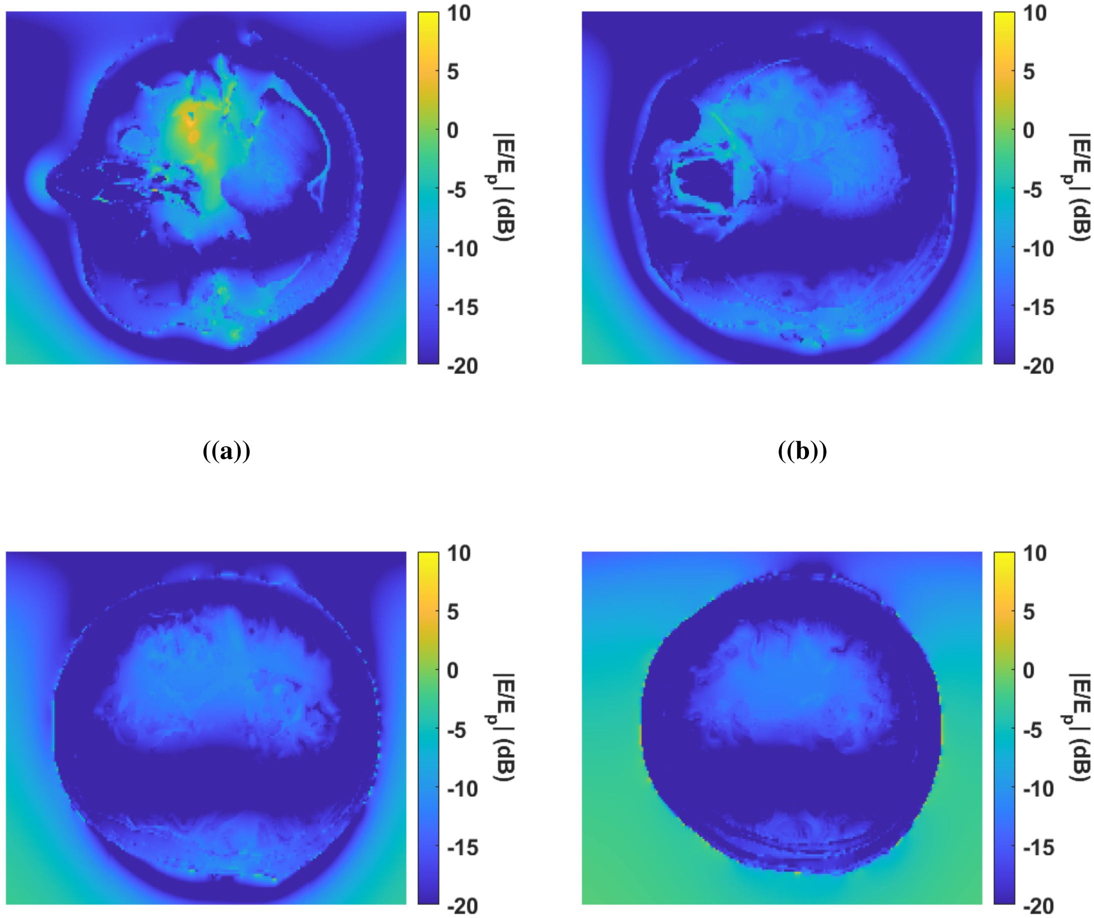

((a)) ((b)) ((c)) ((d))

Figure 4.5: Electric field amplitude relative to the incident plane wave(LFM1) within the MIDA model simulated in OU-FDTD. Shown at various cross-sectional views. (a) Coplanar with the ear canal. (b) 25mm up from the ear canal. (c) 50mm up from the ear canal. (d) 75mm up from the ear canal.

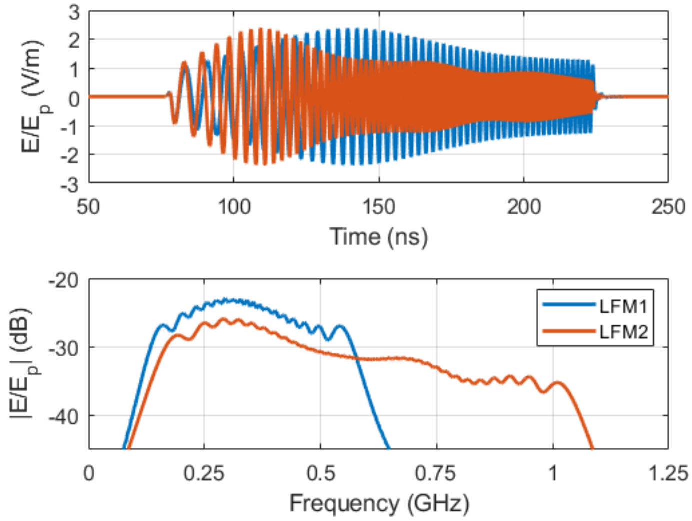

Figure 4.6: Electric field amplitude relative to the incident plane wave within the MIDA model simulated in OU-FDTD. Point-sensor located in fat tissue. Results from LFM1 and LFM2.

The MIDA model was simulated again with LFM2, which contained frequencies up to 1.1GHz. The time-domain and frequency-domain results of this simulation are given in Figure 4.6, which align with the simulated results of LFM1 in their shared frequency range. Both waveforms experience a peak amplitude in the frequency range of 240-380MHz. As LFM2 sweeps across a wider bandwidth than LFM1 in the same time, it will reach its amplitude peak sooner in the time-domain. Figure 4.7(a)-(d) demonstrates that as the electromagnetic wave travels through the head, the high electric field amplitudes remain largely constrained to side of the head the plane wave is incident upon.

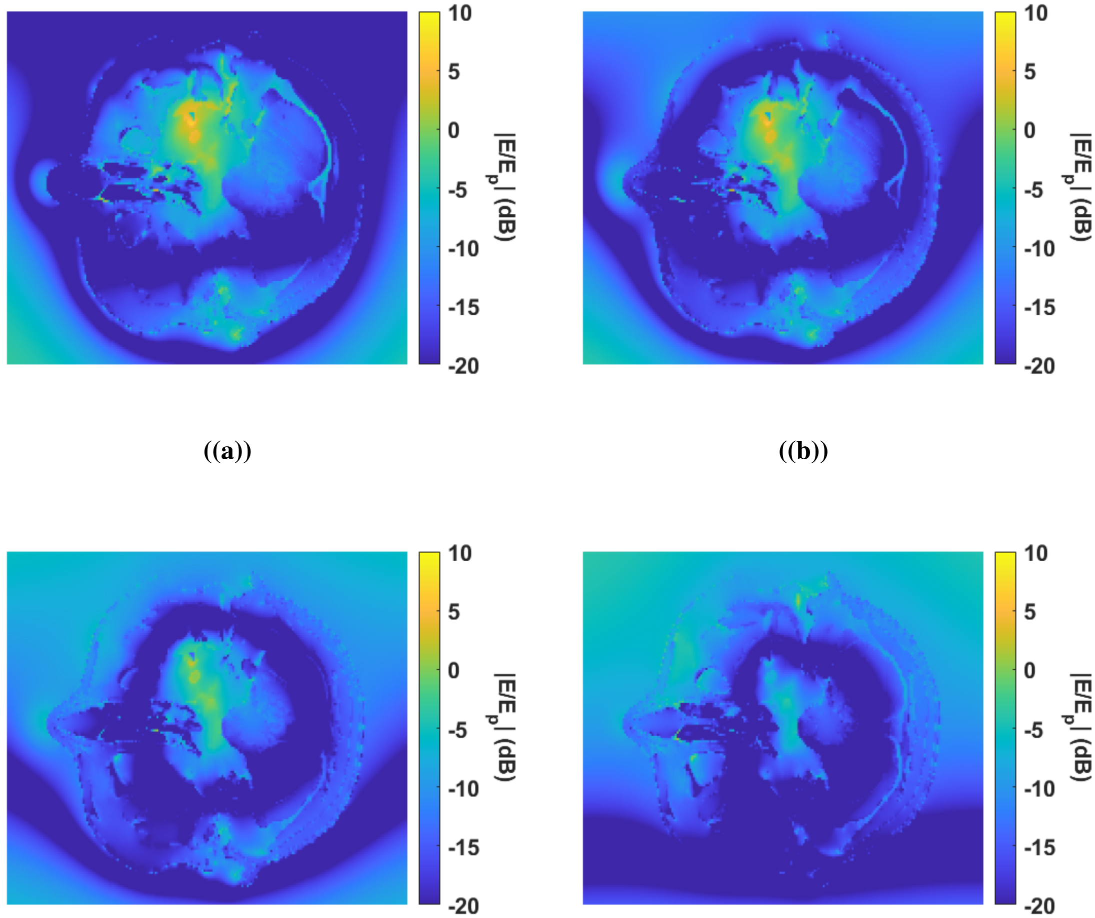

((a)) **((b))** **((c))** **((d))**

Figure 4.7: Electric field amplitude relative to the incident plane wave within the MIDA model simulated in OU-FDTD. Shown at various time-steps throughout the simulation of LFM2. (a) t = 109.2 ns. (b) t = 109.6 ns. (c) t = 109.9 ns. (d) t = 110.3 ns.

The MIDA model was simulated with LFM2 in XFDTD to compare with the results obtained in OU-FDTD. The same focusing phenomena was present in the XFDTD simulation. However, from Figure 4.8, we see that the XFDTD simulation features higher electric field amplitudes across a larger region. There are two factors that play into this: (1) as mentioned in the Simuation Methodology section, the dielectric profiles for fat tissue used by XFDTD and OU-FDTD differ. (2) XFDTD implements frequency dependent dielctrics through a four-term Cole-Cole model. While the Ireland paper offers the field update algorithm given in Equation 4.6 that implements the two-term Debye model, similar documentation does not exist for XFDTD's four-term Cole-Cole model.

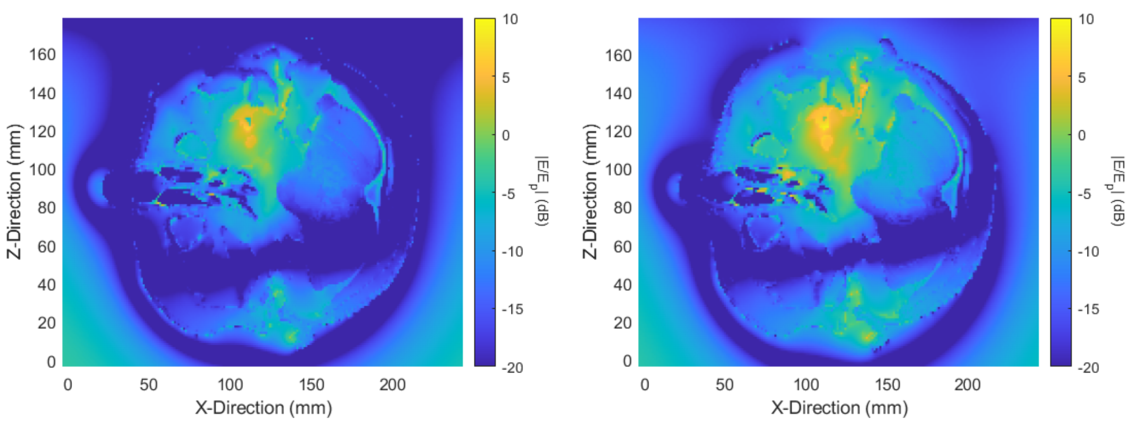

((a)) ((b))

Figure 4.8: Electric field amplitude relative to the incident plane wave(LFM2) within the MIDA model simulated in OU-FDTD and XFDTD. Shown at time-step of peak amplitude. (a) OU-FDTD. (b) XFDTD.

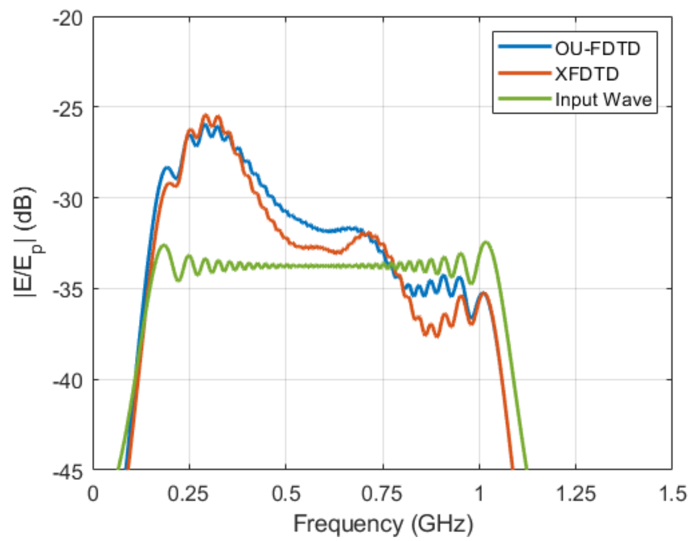

Figure 4.9: Electric field amplitude relative to the incident plane wave(LFM2) within the MIDA model simulated in OU-FDTD and XFDTD. Point-sensor located in adipose tissue.

In the frequency domain, both OU-FDTD and XFDTD show electric field amplitudes greater than the incident plane wave from 150-775 MHz, with an amplitude peak in the range of 240-380 MHz as seen in Figure 4.9.

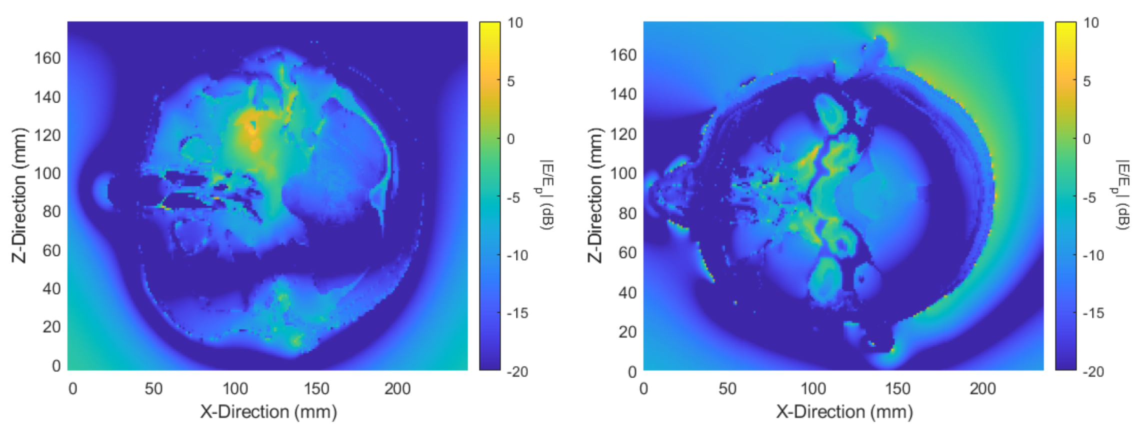

Figure 4.10: Electric field amplitude relative to the incident plane wave(LFM2) within the MIDA and Duke models simulated in OU-FDTD. Shown at time-step of peak amplitude. (a) MIDA. (b) Duke.

Simulations of the Duke phantom also revealed areas where the electric field strength exceeded the maximum amplitude of the incident plane wave, with notable differences from the MIDA phantom. Whereas MIDA results see high field amplitudes focused in a region on the side of the head the plane wave is incident upon, in Duke this effect is scattered around more central parts of the head. This is likely due to the differences in size, shape, and tissue locations between the two phantoms. Adipose tissue is a large proponent of the focusing effect seen in the MIDA simulations – noting Figure 4.2 once again, the Duke model lacks adipose tissue in this region of the head. Instead, the high field amplitudes are constrained to cortical bone tissue. The high field amplitudes being located in the center of the Duke model, as opposed to focused on one side as in MIDA, may be due to its more uniform head shape. Similar to the results of the MIDA simulations, this focusing effect was not present throughout other regions of the head as shown in Figure 4.11. As the plane wave passes through the Duke head model, we again see that the high field strengths only occur in the center region (Figure 4.12).

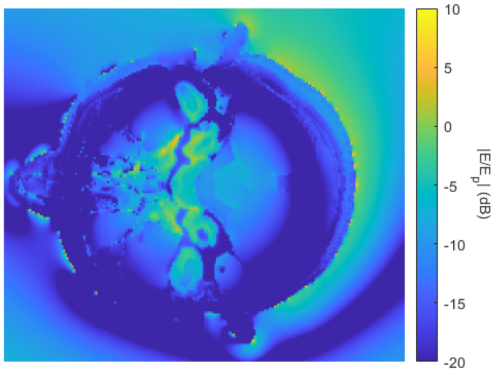

((a))

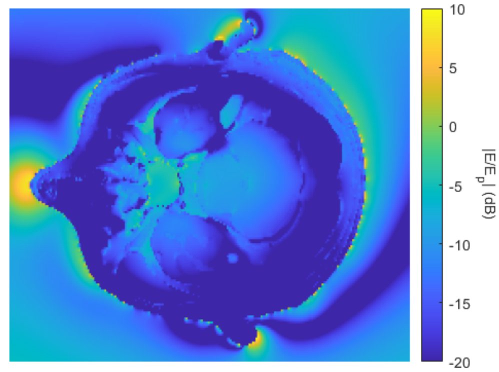

((b))

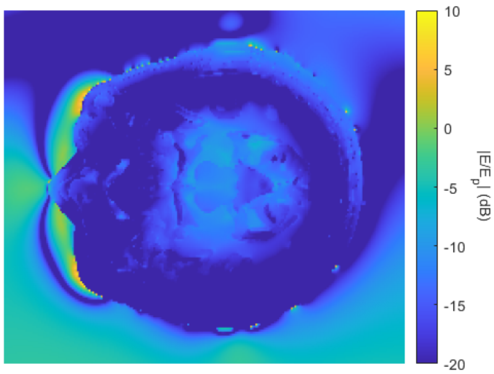

((c))

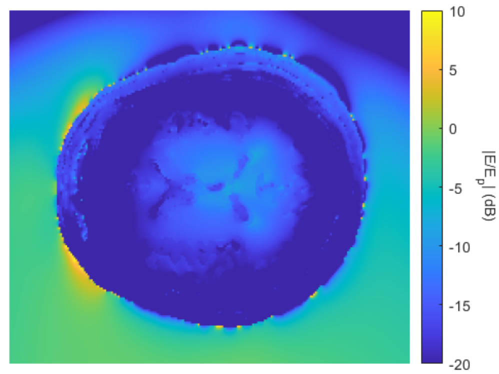

((d))

Figure 4.11: Electric field amplitude relative to the incident plane wave(LFM2) within the Duke model simulated in OU-FDTD. Shown at various cross-sectional views. (a) Coplanar with the ear canal. (b) 25mm up from the ear canal. (c) 50mm up from the ear canal. (d) 75mm up from the ear canal.

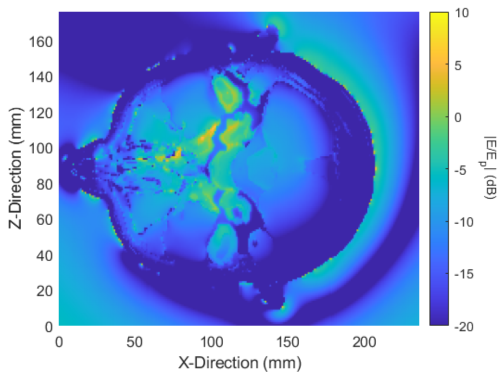

((a))

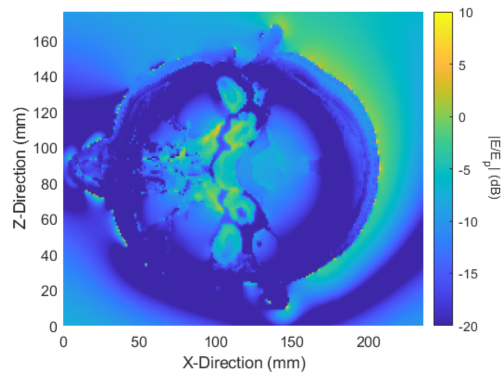

((b))

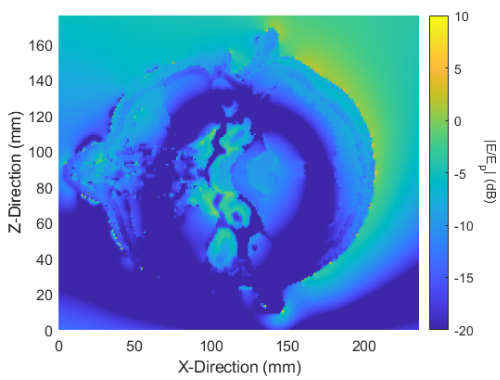

((c))

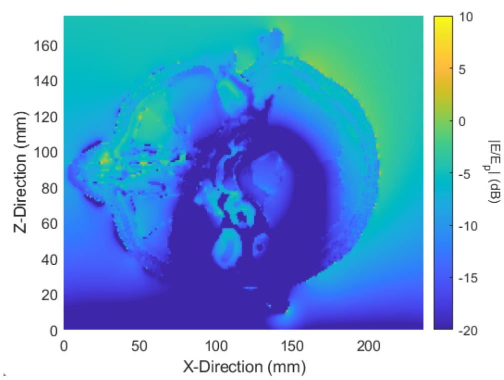

((d))

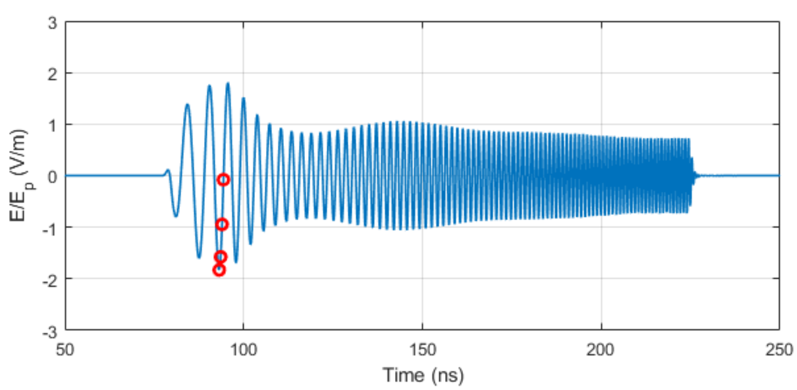

((e))

Figure 4.12: Electric field amplitude relative to the incident plane wave within the Duke model simulated in OU-FDTD. Shown at various time-steps throughout the simulation of LFM2. (a) t = 93.2 ns. (b) t = 93.6 ns. (c) t = 94.0 ns. (d) t = 94.4 ns. (e) Electric field amplitude relative to the incident plane wave at a point sensor located within fat tissue. Red markers indicate the time-steps shown in panels (a)-(d).

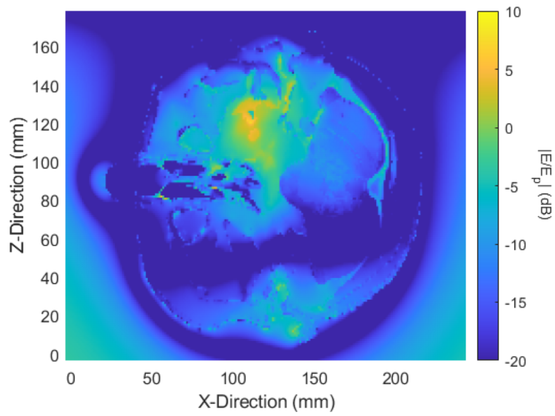

((a))

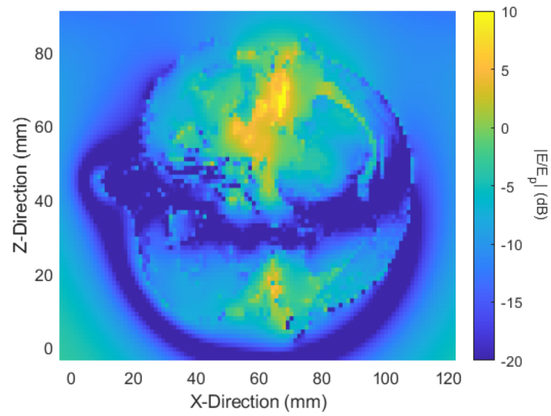

((b))

Figure 4.13: Electric field amplitude relative to the incident plane wave(LFM2) within the full-size and half-size MIDA model simulated in OU-FDTD. Shown at time-step of peak amplitude. (a) Full-size. (b) Half-size.

Given the frequency dependence of this focusing effect as shown in Figure 4.9, it was hypothesized that by shrinking the MIDA phantom to half of its size, the frequency peak would shift upwards by a factor of two. This transformation was carried out, reducing the MIDA phantom's circumference from approximately 50cm to 25cm. A comparison between the full-size and half-size head models is shown in Figure 4.13. The smaller head phantom experienced higher field amplitudes in general throughout its entirety, and the region of tissues with field amplitudes larger than the incident plane wave expanded. Interestingly, the physical location of the peak amplitude in the smaller model shifted from adipose tissue behind the cheek bone, to the pharyngotympanic tube. Additionally, the effect was more prominent in the ear canal opposite the incident plane wave. In Figure 4.14(b), there is a noticeable region of higher than unity field amplitude in the the orbital adipose tissue.

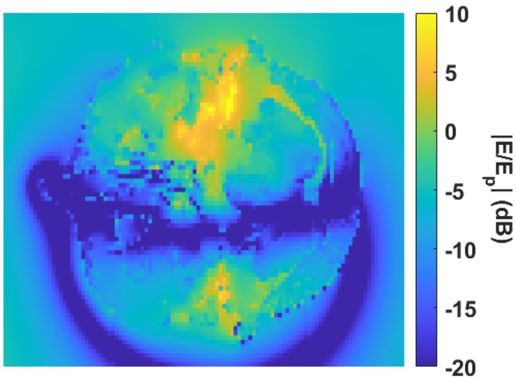

((a))

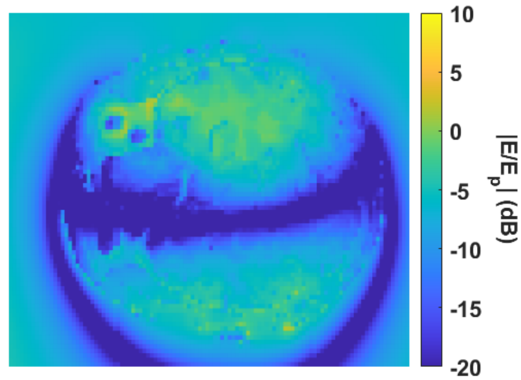

((b))

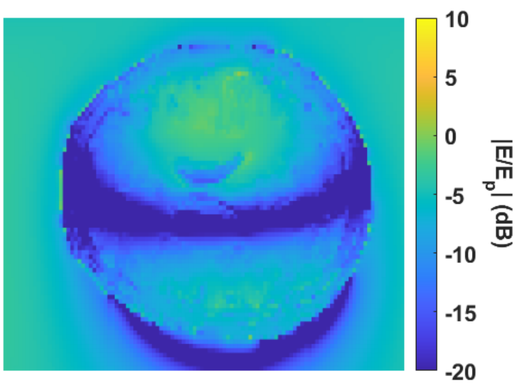

((c))

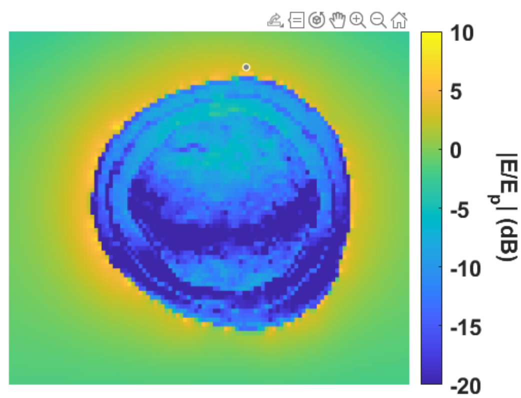

((d))

Figure 4.14: Electric field amplitude relative to the incident plane wave(LFM2) within the half-size Mida model simulated in OU-FDTD. Shown at various cross-sectional views. (a) Coplanar with the ear canal. (b) 17mm up from the ear canal. (c) 34mm up from the ear canal. (d) 51mm up from the ear canal.

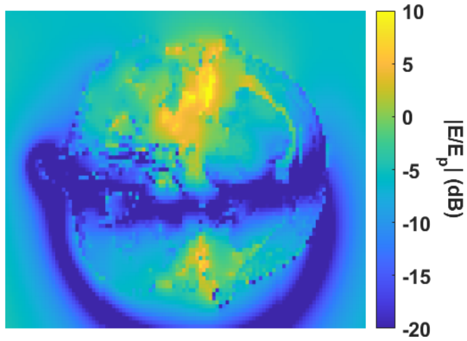

((a))

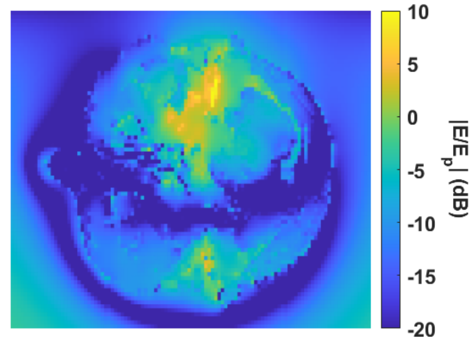

((b))

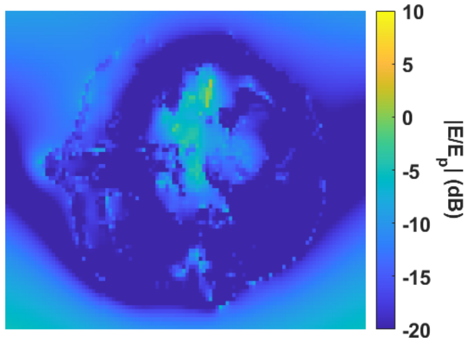

((c))

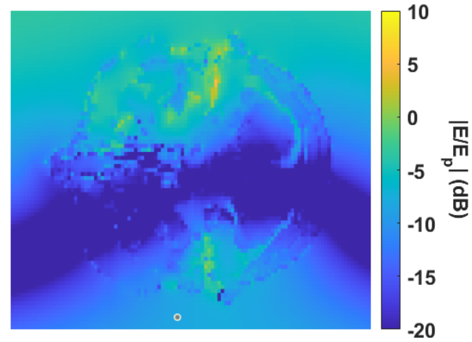

((d))

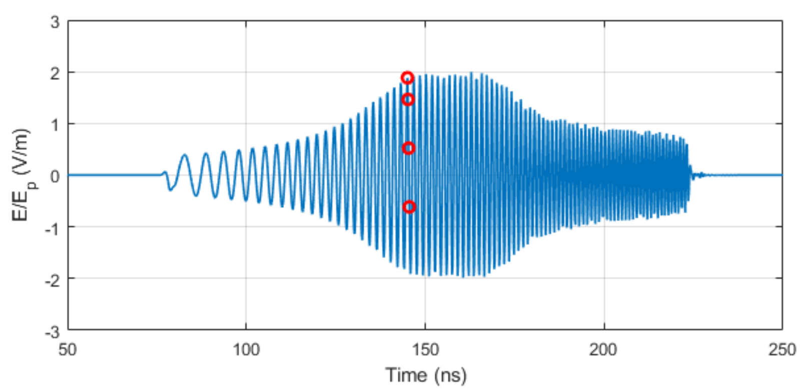

((e))

Figure 4.15: Electric field amplitude relative to the incident plane wave within the half-size MIDA model simulated in OU-FDTD. Shown at various time-steps throughout the simulation of LFM2. (a) t = 145.03 ns. (b) t = 145.20 ns. (c) t = 145.37 ns. (d) t = 145.50 ns. (e) Electric field amplitude relative to the incident plane wave at a point sensor located within adipose tissue. Red markers indicate the time-steps shown in panels (a)-(d).

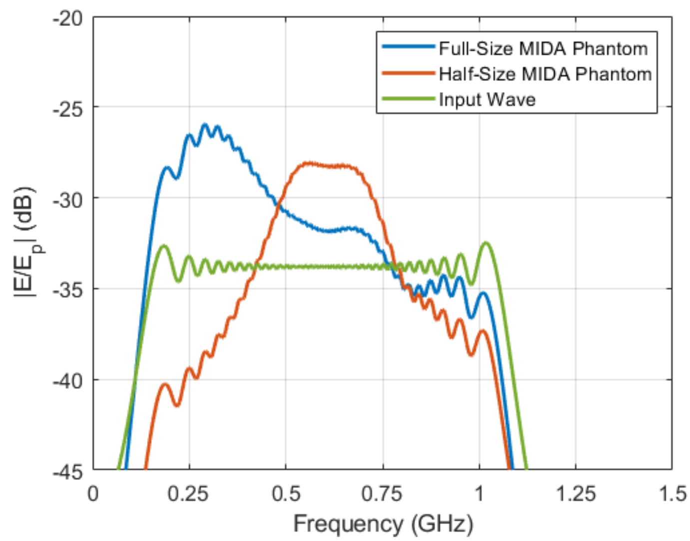

Figure 4.16: Electric field amplitude relative to the incident plane wave(LFM2) within the full-size and half-size MIDA models simulated in OU-FDTD. Point-sensor located in adipose tissue.

The frequency range of the amplitude peak in the half-size MIDA phantom shifted upwards by nearly 2, in the range of 545-680 MHz. At both head sizes however, the amplitude falls below that of the incident plane wave at 775 MHz.

4.3 Discussion

While the "focusing" effect shown in this chapter is certainly a fascinating result, it also most certainly requires additional validation before being considered a realizable physical phenomena. All of the results shown here come from the same numerical method - FDTD, albeit with different methods for modeling dispersive materials. Presuming the results are accurate however, there are some interesting things to take note of.

Firstly, It is well studied that dielectric properties vary by age, sex, and by individual [38], [39]. The only difference between OU-FDTD and XFDTD is how each solver modeled dispersive materials - spatial step sizes and time step sizes between the two are identical for all simulations in this chapter. The comparison between OU-FDTD and XFDTD for the MIDA phantom, then indicates that variance in the dielectric properties will have a significant impact on the magnitude of the effect.

Secondly, the comparison between the MIDA and Duke phantoms demonstrate that anatomical differences – such as the shape of the head, or whether there is more fat or muscle tissue present – also play a role in how this focusing manifests. It also indicates the need for additional head phantoms with anatomical detail on the order of the MIDA model.

Lastly, the frequency dependent behavior of this effect is inversely proportional to the size of the head as seen by the comparison between the full-size and half-size MIDA phantoms.

Chapter 5

Conclusions and Future Work

5.1 Conclusions

The general construction of an FDTD solver was presented in this thesis, and applied to two vastly different problems in electromagnetics. The need for full wave electromagnetic solvers capable of realizing non-LTI antenna designs was addressed, and a method for implementing time-varying components directly as lumped components demonstrated. The limited capabilities of current commercial solvers in this regard was discussed, as well as the trade-offs between time-domain and frequency-domain techniques. It was found that for high resolution head phantoms, there is a focusing effect for frequencies at the low end of the UHF band wherein electric field amplitudes inside specific regions of the human head will exceed that of the incident plane wave. The different parameters that may influence this effect were also discussed.

5.2 Scientific Impact

- Provided a novel method for implementing an ideal time-varying capacitor in the FDTD method and validated it against results from two commercial time-domain solvers and a frequency-domain solver.

- Evaluated the usability of two popular commercial time-domain solvers for non-LTI antenna research.
- FDTD simulation revealed a focusing effect within the head for incident plane waves at the lower end of UHF.
- Demonstrated the importance of head phantom fidelity in the analysis of RF impacts on human tissue.

5.3 Future Work

For non-LTI antenna design, it was found that the FDTD method was poorly suited for simulating parameter sweeps for narrowband designs due to the simulation runtimes required. In its general form, FDTD is an explicit method that is conditionally stable, which enforces a stability requirement on the time step size. As the time step size required by stability is often much larger than the time step size required by accuracy, an unconditionally stable FDTD method could be explored to circumvent this shortcoming. This typically requires an implicit numerical scheme to be implemented, which in turn increases the computational complexity. An unconditionally stable FDTD method could also be useful for recreating the human head simulations in Chapter 4 with several pulses. The analysis begun in Chapter 4 could be continued down a number of different avenues. Validation of the results, either with a different type of solver entirely – such as an FEMTD solver – or experimentally with an artificial head model is a priority. Analyzing the effects of head morphology through the simulation of additional high resolution head phantoms, and running a statistical analysis on the effects of variance in the dielectric properties of human tissue are also appealing avenues to explore. Finally, plane waves with varying angles of incidence and LFM pulses with lower and higher frequency content should also be considered.

References

[1] K. Yee, “Numerical solution of initial boundary value problems involving maxwell’s equations in isotropic media,” *IEEE Transactions on Antennas and Propagation*, vol. 14, no. 3, pp. 302–307, 1966.

[2] L. J. Chu, “Physical limitations of omni-directional antennas,” *Journal of applied physics*, vol. 19, no. 12, pp. 1163–1175, 1948.

[3] H. A. Wheeler, “Fundamental limitations of small antennas,” *Proceedings of the IRE*, vol. 35, no. 12, pp. 1479–1484, 1947.

[4] K. D. Bhakta and Y. E. Wang, “Augmenting the efficiency bandwidth product of electrically small antennas using direct antenna phase modulation,” in *2024 IEEE International Symposium on Antennas and Propagation and INC/USNC-URSI Radio Science Meeting (AP-S/INC-USNC-URSI)*, 2024, pp. 2391–2392.

[5] Z. Fritts, A. Babaee, S. M. Young, and A. Grbic, “Increasing the efficiency-bandwidth product and impedance bandwidth of electrically-small antennas through parametric space-time variation,” in *2024 18th European Conference on Antennas and Propagation (EuCAP)*, 2024, pp. 1–4.

[6] E. Slevin, M. B. Cohen, N. Opalinski, L. Thompson, and M. Golkowski, “Broadband electrically small vlf/lf transmitter via time-varying antenna properties,” *IEEE Transactions on Antennas and Propagation*, vol. 70, no. 1, pp. 97–110, 2022.

[7] J. P. Santos, F. Fereidoony, Y. Huang, and Y. E. Wang, “High bandwidth electrically small antennas through bfsk direct antenna modulation,” in *MILCOM 2018 - 2018 IEEE Military Communications Conference (MILCOM)*, 2018, pp. 1–9.

[8] D. S. S. Corp, “Cst studio,” 2024. [Online]. Available: https://www.3ds.com/products/simulia/cst-studio-suite

[9] Remcom, "Xfdtd," 2024. [Online]. Available: https://www.remcom.com/xfdtd-3d-em-simulation-software

[10] S. F. Bass, A. M. Palmer, K. R. Schab, K. C. Kerby-Patel, and J. E. Ruyle, "Conversion matrix method of moments for time-varying electromagnetic analysis," *IEEE Transactions on Antennas and Propagation*, vol. 70, no. 8, pp. 6763–6774, 2022.

[11] M. A. Al-alaa, H. A. Elsadek, and E. A. Abdallah, "Effects of human head on frequency reconfigurable pifa antenna performance and sar calculations," in *2015 IEEE MTT-S International Conference on Numerical Electromagnetic and Multiphysics Modeling and Optimization (NEMO)*, 2015, pp. 1–3.

[12] D. Gombarska, Z. Psenakova, and A. Gajdosova, "Numerical model of realistic human head phantom," in *2022 23rd International Conference on Computational Problems of Electrical Engineering (CPEE)*, 2022, pp. 1–4.

[13] M. E. Karim and A. B. M. Aowlad Hossain, "Sar analysis of human head model using common antennas of 4g lte mobile communications," in *2021 Fourth International Conference on Electrical, Computer and Communication Technologies (ICECCT)*, 2021, pp. 1–5.

[14] L. Belrhiti, F. Riouch, A. Tribak, J. Terhzaz, A. Bouyahyaoui, and A. M. Sanchez, "Comparison and evaluation of sar induced in four human head models for two types of antennas used in mobile telephones," in *2018 6th International Conference on Multimedia Computing and Systems (ICMCS)*, 2018, pp. 1–6.

[15] S. Gabriel, R. W. Lau, and C. Gabriel, "The dielectric properties of biological tissues: Iii. parametric models for the dielectric spectrum of tissues," *Physics in Medicine Biology*, vol. 41, no. 11, p. 2271, nov 1996. [Online]. Available: https://dx.doi.org/10.1088/0031-9155/41/11/003

[16] A. Taflove, "Application of the finite-difference time-domain method to sinusoidal steady-state electromagnetic-penetration problems," *IEEE Transactions on Electromagnetic Compatibility*, vol. EMC-22, no. 3, pp. 191–202, 1980.

[17] D. Sullivan, O. Gandhi, and A. Taflove, "Use of the finite-difference time-domain method for calculating em absorption in man models," *IEEE Transactions on Biomedical Engineering*, vol. 35, no. 3, pp. 179–186, 1988.

[18] X. Zhang, J. Fang, K. K. Mei, and Y. Liu, “Calculations of the dispersive characteristics of microstrips by the time-domain finite difference method,” *IEEE Transactions on Microwave Theory Techniques*, vol. 36, no. 2, pp. 263–267, Feb. 1988.

[19] T. Kashiwa and I. Fukai, “A treatment by the fd-td method of the dispersive characteristics associated with electronic polarization,” *Microwave and Optical Technology Letters*, vol. 3, no. 6, pp. 203–205, 1990. [Online]. Available: https://onlinelibrary.wiley.com/doi/abs/10.1002/mop.4650030606

[20] J. Maloney, G. Smith, and W. Scott, “Accurate computation of the radiation from simple antennas using the finite-difference time-domain method,” *IEEE Transactions on Antennas and Propagation*, vol. 38, no. 7, pp. 1059–1068, 1990.

[21] D. Katz, M. Piket-May, A. Taflove, and K. Umashankar, “Fdtd analysis of electromagnetic wave radiation from systems containing horn antennas,” *IEEE Transactions on Antennas and Propagation*, vol. 39, no. 8, pp. 1203–1212, 1991.

[22] W. Sui, D. Christensen, and C. Durney, “Extending the two-dimensional fdtd method to hybrid electromagnetic systems with active and passive lumped elements,” *IEEE Transactions on Microwave Theory and Techniques*, vol. 40, no. 4, pp. 724–730, 1992.

[23] S. M. Smith and C. Furse, “Stochastic fdtd for analysis of statistical variation in electromagnetic fields,” *IEEE Transactions on Antennas and Propagation*, vol. 60, no. 7, pp. 3343–3350, 2012.

[24] Y. Taniguchi, Y. Baba, N. Nagaoka, and A. Ametani, “An improved thin wire representation for fdtd computations,” *IEEE Transactions on Antennas and Propagation*, vol. 56, no. 10, pp. 3248–3252, 2008.

[25] R. M. S. de Oliveira and R. R. Paiva, “Least squares finite-difference time-domain,” *IEEE Transactions on Antennas and Propagation*, vol. 69, no. 9, pp. 6111–6115, 2021.

[26] A. Taflove and S. C. Hagness, *Computational electrodynamics: the finite-difference time-domain method*, 3rd ed. Norwood: Artech House, 2005.

[27] R. Holtzman and R. Kastner, “The time-domain discrete green’s function method (gfm) characterizing the fdtd grid boundary,” *IEEE Transactions on Antennas and Propagation*, vol. 49, no. 7, pp. 1079–1093, 2001.

[28] J.-P. Berenger, "A perfectly matched layer for the absorption of electromagnetic waves," *Journal of Computational Physics*, vol. 114, no. 2, pp. 185–200, 1994. [Online]. Available: https://www.sciencedirect.com/science/article/pii/S0021999184711594

[29] F. T. Ulaby, *Fundamentals of applied electromagnetics*. Upper Saddle River, NJ, USA: Prentice-Hall, Inc., 1997.

[30] T. Weiland, "A discretization model for the solution of Maxwell's equations for six-component fields," *Archiv Elektronik und Uebertragungstechnik*, vol. 31, pp. 116–120, Apr. 1977.

[31] G. Fisher and J. Connelly, "Modeling time-dependent elements for spice transient analyses," *IEEE Transactions on Computer-Aided Design of Integrated Circuits and Systems*, vol. 5, no. 3, pp. 429–432, 1986.

[32] M. Capek, P. Hazdra, V. Adler, P. Kadlec, V. Sedenka, M. Marek, M. Masek, V. Losenicky, M. Strambach, M. Mazanek, and J. Rymus, "Atom: A versatile matlab tool for antenna synthesis," in *12th European Conference on Antennas and Propagation (EuCAP 2018)*, 2018, pp. 1–5.

[33] "Iec/ieee international standard – determining the peak spatial-average specific absorption rate (sar) in the human body from wireless communications devices, 30 mhz to 6 ghz - part 1: General requirements for using the finite-difference time-domain (fdtd) method for sar calculations," *IEC/IEEE 62704-1:2017*, pp. 1–86, 2017.

[34] D. Ireland and A. Abbosh, "Modeling human head at microwave frequencies using optimized debye models and fdtd method," *IEEE Transactions on Antennas and Propagation*, vol. 61, no. 4, pp. 2352–2355, 2013.

[35] C. B. E. N. B. L. M. G. D. P. A. K. N. K. PA Hasgall, F Di Gennaro, "It'is database for thermal and electromagnetic parameters of biological tissues version 4.1," February 2022. [Online]. Available: itis.swiss/database

[36] M. I. Iacono, E. Neufeld, E. Akinnagbe, K. Bower, J. Wolf, I. Vogiatzis Oikonomidis, D. Sharma, B. Lloyd, B. J. Wilm, M. Wyss, K. P. Pruessmann, A. Jakab, N. Makris, E. D. Cohen, N. Kuster, W. Kainz, and L. M. Angelone, "Mida: A multimodal imaging-based detailed anatomical model of the human head and

neck," *PLOS ONE*, vol. 10, no. 4, pp. 1–35, 04 2015. [Online]. Available: https://doi.org/10.1371/journal.pone.0124126

[37] A. Christ, W. Kainz, E. G. Hahn, K. Honegger, M. Zefferer, E. Neufeld, W. Rascher, R. Janka, W. Bautz, J. Chen, B. Kiefer, P. Schmitt, H.-P. Hollenbach, J. Shen, M. Oberle, D. Szczerba, A. Kam, J. W. Guag, and N. Kuster, "The virtual family—development of surface-based anatomical models of two adults and two children for dosimetric simulations," *Physics in Medicine Biology*, vol. 55, no. 2, p. N23, dec 2009. [Online]. Available: https://dx.doi.org/10.1088/0031-9155/55/2/N01

[38] E. Conil, A. Hadjem, F. Lacroux, M. F. Wong, and J. Wiart, "Variability analysis of sar from 20 mhz to 2.4 ghz for different adult and child models using finite-difference time-domain," *Physics in Medicine Biology*, vol. 53, no. 6, p. 1511, feb 2008. [Online]. Available: https://dx.doi.org/10.1088/0031-9155/53/6/001

[39] C. Gabriel and A. Peyman, "Dielectric measurement: error analysis and assessment of uncertainty," *Physics in Medicine Biology*, vol. 51, no. 23, p. 6033, oct 2006. [Online]. Available: https://dx.doi.org/10.1088/0031-9155/51/23/006